Small-Signal and Transient Stability Analysis of Voltage-Source Converters

by

Heng Wu

Department of Energy Technology

Aalborg University, Denmark

AALBORG UNIVERSITY
DENMARK

Dissertation submitted April, 2020

Thesis submitted: April, 2020
PhD supervisor: Prof. Xiongfei Wang,
Aalborg University

PhD committee: Prof. Francesco Iannuzzo (chairman)
Aalborg University

Prof. Paolo Mattavelli
University of Padova

Prof. Tim Green
Imperial College London

PhD Series: Faculty of Engineering and Science, Aalborg University

ISSN: xxxx- xxxx
ISBN: xxx-xx-xxxx-xxx-x

Published by:
Aalborg University Press
Skjernvej 4A, 2nd floor
DK – 9220 Aalborg Ø
Phone: +45 99407140
aauf@forlag.aau.dk
forlag.aau.dk

Printed in Denmark by Rosendahls, 2015

English summary

Voltage-source converters (VSCs) have been widely used with power generation, transmission, distribution and consumption. The full power controllability of VSCs enables to modernize the electric power grid with more flexibility, yet it also poses new challenges to the stable operation of power systems.

In the low-voltage distribution network, VSCs with capacitors centralized in the DC-link, e.g., two-/three-level VSCs, are commonly used. In contrast, modular multilevel converters (MMCs) with capacitors distributed in each submodule, are typically adopted in the high-voltage transmission grid. Differing from two-/three-level VSCs, whose small-signal stability has been extensively investigated in the literature, less research works can be found on the small-signal stability of MMCs. The internal dynamics of the MMC, i.e., capacitor voltage variations of submodules, tends to affect its external ac dynamics and leads to the frequency-coupling behavior, which not only complicates its small-signal model, but also brings in new challenges for the stability analysis and the controller design of the MMC system.

To cope with these issues, a systematic modeling framework of the MMC is developed in this PhD project based on the harmonic state space modeling theory and complex space vectors, which is capable of capturing the frequency-coupling dynamics of the MMC. The small-signal models for MMCs with grid-forming (GFM) control and grid-following (GFL) control are developed, based on which, the differences and similarities between the models of MMCs and two-/three-level VSCs are highlighted, and root causes of different instability phenomena of MMCs are revealed. Lastly, perspectives on control methods and design recommendations for stabilizing MMCs in different operating scenarios are given.

Besides the small-signal stability, the transient stability of grid-connected VSCs, i.e., the synchronization stability under large disturbances, is also addressed in this thesis. The transient stability analysis is more challenging, due to the necessity of considering the large-signal nonlinear dynamics of synchronization loops, e.g., the active power loop (APL) for GFM-VSCs and the phase-locked loop (PLL) for GFL-VSCs. To tackle these challenges, the phase portrait is employed for a design-oriented analysis on the transient stability of GFM- and GFL-VSCs, with which, the main cause for the loss of synchronization of VSCs under large disturbances is identified. Further, it is found that the transient stability of VSCs can be guaranteed by using the first-order synchronization loop, i.e., the first-order APL for GFM-VSCs or the first-order PLL for GFL-VSCs, provided that the equilibrium points exist after disturbances. When there are no equilibrium points during the faults, the VSC with the first-order synchronization loop can still be re-synchronized with the power grid, even if the fault clearing time is beyond the critical clearing time, which reduces the risk of system collapse caused by the delayed fault clearance.

Dansk resume

Frekvensomformere opereret som spændingskilder (VSC'er) er brugt i vid udstrækning til vedvarende energiproduktion, energieffektiv energioverførsel, distribution og forbrug. Den fleksible styrbarhed af VSC'er gør det muligt at modernisere det elektriske elnet med mere fleksibilitet, men det medfører også nye udfordringer i forbindelse med at sikre en stabil drift af fremtidens elsystemer.

I modsætning til to-niveau VSC'er, hvis småsignals stabilitet er omfattende undersøgt i eksisterende litteratur, er der foretaget minimal forskning vedrørende småsignals stabilitet af modulære multilevel-konvertere (MMC'er). MMC'ers unikke interne dynamik (kondensatorspændingsvariationer og styrring af cirkulerende strømme) har en tendens til at påvirke dens eksterne vekselstrømsdynamik og medføre en frekvensafhængig koblingsopførsel, som ikke kun komplicerer dens småsignalsmodel, men også medfører nye udfordringer for stabilitetsanalyse og regulatordesign.

For at imødekomme disse problemstillinger har dette ph.d-projekt udviklet en systematisk modelleringsramme for MMC'er baseret på den harmoniske state-space modelleringsteori og den dynamiske repræsentation af komplekse vektorer, som er i stand til at beskrive MMC'ers frekvensafhængige koblingsdynamik. Småsignalsmodeller af MMC'er, der fungerer i ø-drift samt net-tilsluttede tilstande, er også udviklet. Baseret på disse, er forskelle og ligheder mellem modellerne af MMC'erne og to-niveau VSC'erne fremhævet, og grundårsagerne til forskellige ustabiliteter af MMC'er er beskrevet. Til sidst gives der en perspektivering vedrørende kontrolmetoder og designanbefalinger til stabilisering af MMC'er i forskellige driftsscenarier.

Sammenlignet med småsignals stabilitetsundersøgelser er analysen af den transiente stabilitet (stor-signalsstabilitet) af VSC'er mere udfordrende på grund af nødvendigheden af at medtage de ikke-lineære dynamikker i synkroniseringssløjfer, dvs. regulering af aktiv effekt (APL) for net-skabende VSC'er, samt fasesynkroniseringsregulering (PLL) for net-følgende VSC'er. For at imødekomme disse udfordringer tager dette ph.d.-projekt faseportretter i brug for at karakterisere den transiente stabilitet af net-skabende og net-følgende VSC'er. Her er det den ikke-lineære synkroniseringsdynamik der er identificeret som hovedårsag til ustabilitet, ved store forstyrrelser i nettet. Det er dog vist, at den transiente stabilitet af VSC'erne kan forbedres ved at bruge en første ordens synkroniseringssløjfe, dvs. en første ordens APL til net-skabende VSC'er eller en første ordens PLL til net-følgende VSC'er. Ved brug af dette kan den transiente stabilitet af VSC'er garanteres, forudsat at der findes ligevægtspunkterne efter forstyrrelserne. Desuden medfører dette også, at det er muligt for VSC'er at synkronisere med elnettet, selvom fejlrydningstiden er

længere end den kritiske aktueringsstid. Alt dette reducerer risikoen for at el-nettet bryder sammen.

Acknowledgements

This PhD project is carried out in the Department of Energy Technology, Aalborg University. First of all, I would like to express my sincere gratitude to my supervisor, Prof. Xiongfei Wang, for the time he spent during my PhD study. I really benefit a lot from his insightful and patient guidance. I am also very grateful for the opportunity he gave me to be deeply involved in the discussion and corporation with the industry. I feel happy and honored that the outcome of this PhD project could add values to the practice, but I know it would not be possible without his help and support.

I would like to thank Dr. Łukasz Kocewiak for inviting me for the research stay in Ørsted Wind Power, the industrial-oriented research carried out in Ørsted has deepened my understanding for the practical challenges faced by the real world. I would also like to thank Prof. Rainer Marquardt, Prof. Claus Hillermeier, Dr. Jose-Luis Marques-Lopez and Mr. Daniel Dinkel, for the fruitful discussion during my study abroad in Bundeswehr University Munich, Germany. It is really interesting to learn the nonlinear control of modular multilevel converters.

Special thanks go to Prof. Dongsheng Yang, I feel so lucky to be able to work with him during my entire master and PhD studies. Apart from the knowledge and methodology learnt from him, I am very grateful for his encouragement and support during my hard times, which are really helpful for me to overcome the difficulties.

I would also like to thank all members in the egrid research programme, especially to Yicheng, Hong and Mads Graungaard Taul, for the extensive discussion and collaboration in the research project. I would like to thank all my colleagues and staffs at the Department of Energy Technology, Aalborg University, for their kind support during my PhD studies.

Last but not least, I would like to express my deepest gratitude to my family for their endless love, support and understanding. They have no idea of what my research is about, but always encourage me to pursue my own dream.

This PhD project is supported by Aalborg University Strategic Talent Management Programme, and industrial projects funded by TenneT TSO GmbH and NR Electric Co., Ltd. I would like to express my grateful acknowledgement to these financial support.

Heng Wu

Aalborg University, March, 2020

Table of contents

Table of figures

Chapter 1. Introduction

1.1. Background and Challenge

Power system stability has been identified as one of the key challenges for the secure and reliable operation of the system [1]-[2]. The research on different stability issues regard synchronous generators (SGs) dominated power system has lasted for centuries and abundant research results are readily available [1]-[2]. Yet, today's modern power system is evolving with the increasing replacement of SGs with power electronic converters [3]. Differing from SGs, the dynamic behavior of power electronic converters is highly affected by the control algorithms. The converter-grid interactions have led to a number of stability related incidents ranging from the harmonic stability to the loss of synchronization (LOS), which are not foreseen by the traditional power system stability analysis [4]-[7]. Hence, it is of vital importance to reinvestigate the stability of the modern power system by fully considering the dynamics of power electronic converters [8]-[9].

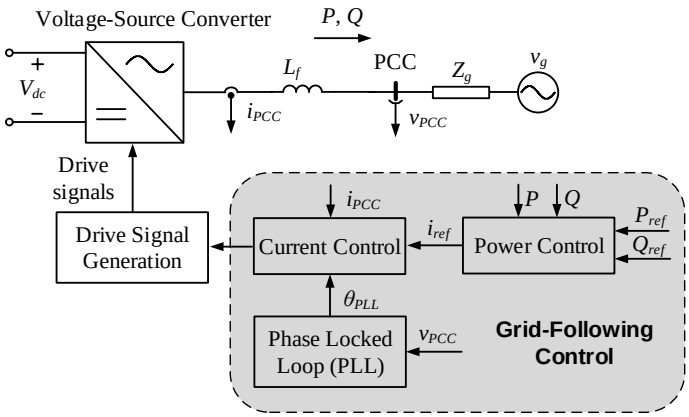

(a)

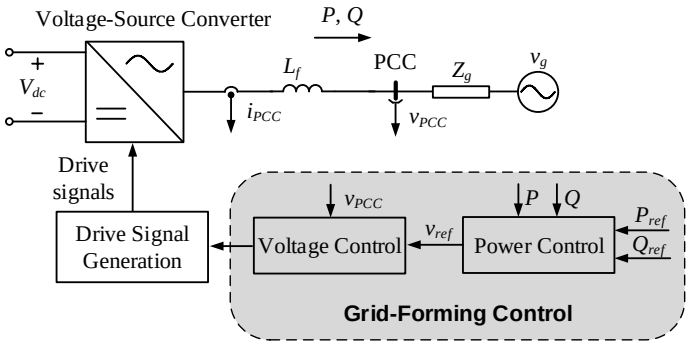

(b)

Figure 1.1. Typical control architectures of VSCs. (a) GFL-VSCs. (b) GFM-VSCs.

Fig. 1.1 shows two basic control architectures of voltage-source converters (VSCs), i.e., grid-following (GFL) VSCs and grid-forming (GFM) VSCs. The GFL-VSC is controlled as a current source while the GFM-VSC is controlled as a voltage source [10]-[11]. Hence, GFM-VSCs can be operated in both the stand-alone and the grid-connection mode [10], while GFL-VSCs can only be operated in the grid-connection mode [11]. For the grid-connected operation, GFM-VSCs are synchronized with the power grid by means of the active power loop (APL) [10], while the phase-locked loop (PLL) is adopted for GFL-VSCs for the grid synchronization [11]. Regardless of the used control schemes, the dynamics of VSCs is highly nonlinear [8], which challenges the system modeling and stability analysis. The nonlinear models of VSCs can be linearized around their operating points for the small-signal stability studies [8]. In contrast, for the transient stability studies that focus on the synchronization stability of VSCs under large disturbances, the nonlinear model of VSCs should be used [12]-[13].

1.1.1. Small-Signal Stability

In the low-voltage distribution network, the VSCs with capacitors centralized in the DC-link, e.g., two-/three-level VSCs, are commonly used for the integration of renewable energy resources like the solar and wind power plant [11]. In contrast, modular multilevel converters (MMCs) with capacitors distributed in each submodule are typically adopted in the high-voltage transmission grid, such as the high-voltage direct current (HVDC) power systems [14]. The small-signal modeling and stability analysis of two-/three-level VSCs have been extensively addressed in the literature [15]-[18]. In contrast, less research attention has been paid to the small-signal stability of MMCs. Differing from two-/three-level VSCs with centralized DC-link capacitors, whose capacitor voltage ripples are negligible due to the cancellation of oscillating powers within three phases [11], the capacitor voltage ripples of MMCs are more

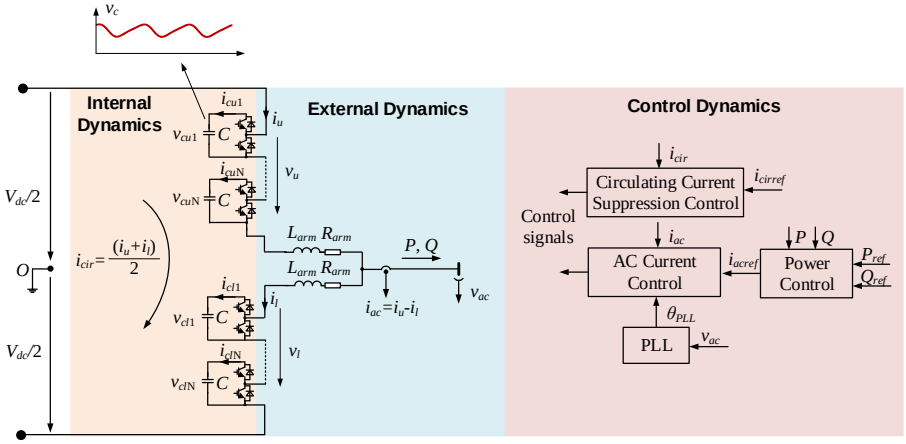

(a)

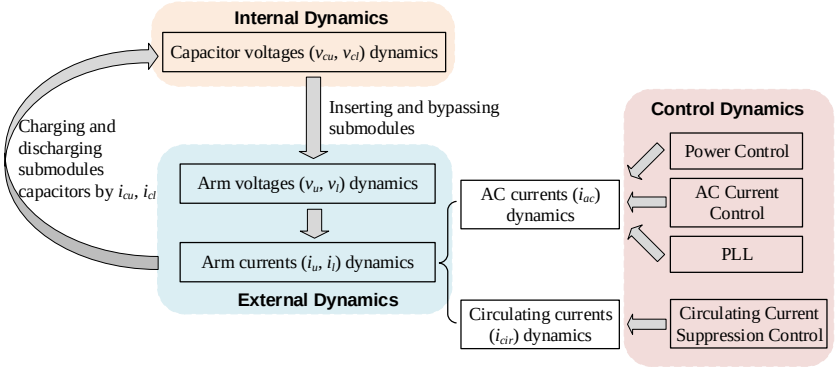

(b)

Figure 1.2. Dynamic couplings of the MMC. (a) System diagram of the GFL-MMC. (b) Illustration of the coupling between the internal, external dynamics of the power stage and the control dynamics of the MMC.

significant, due to the necessity of buffering the single-phase oscillating power [14]. Therefore, the capacitor voltage variation, i.e., the internal dynamics of the MMC, would affect its arm voltages and currents (external ac-dynamics) through inserting and bypassing of submodules, and these external dynamics will in turn affect the current charging and discharging the submodule capacitors [19], as shown in Fig. 1.2. Such interactions lead to a strong coupling between the internal and external dynamics of the power stage of the MMC [19]. More complicated dynamics of the MMC is further introduced by its control loops. As illustrated in Fig. 1.2, the arm current of the MMC can be decomposed into the ac current (i_{ac}) and the circulating current (i_{cir}), whose dynamics are affected by the corresponding control loops. Hence, the control

dynamics of the MMC is coupled with the internal and external dynamics of its power stage, which brings in significant challenges to the small-signal modeling and stability analysis of MMCs [20].

1.1.2. Transient Stability

Comparing with small-signal stability studies, the transient stability analysis of VSCs has not yet drawn too much attention. However, the real incidents on the LOS of wind and photovoltaic power plants during the fault have been increasingly reported [21]-[23]. A field measurement example is given in Fig. 1.3, which illustrates the tripping of Hornsea offshore wind farm during the fault [23]. Hence, not only the small-signal stability, but also the transient stability of VSCs should be guaranteed for the secure and reliable operation of the power system.

The nonlinear dynamic responses of VSCs under large disturbances need to be characterized for transient stability studies. Due to the difficulty in obtaining analytical solutions of nonlinear systems, the electromagnetic transient (EMT) simulations are widely used for the transient stability analysis [12]-[13]. Yet, the EMT simulation results are merely numerical studies based on specific system parameters and operating scenarios, which provide little insight into a general design guideline of VSC control system for ensuring the transient stability.

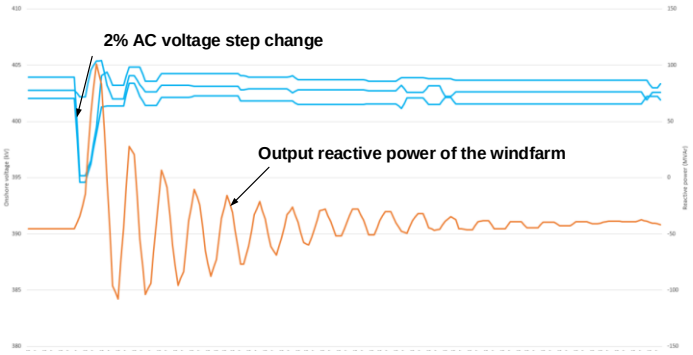

(a)

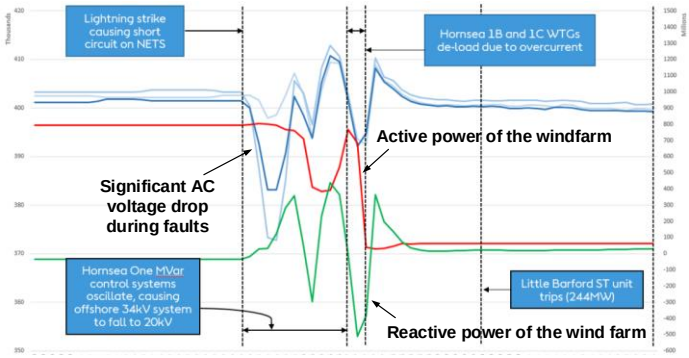

(b)

Figure 1.3. Field measurement waveform of responses of Hornsea offshore windfarm under disturbances. (a) Stable operation after the small-signal disturbance. (b) Unstable operation during the fault. Source: [23].

1.2. State of the Art

1.2.1. Small-Signal Modeling and Stability Analysis of MMCs

In some early works, the impacts of internal dynamics are neglected, and the small-signal model of the power stage of two-/three-level VSCs is directly adopted for that of MMCs [24]-[25]. Yet, this simplification has been proven as inadequate in [26], where the significantly different power stage dynamics between MMCs and two-/three-level VSCs have been revealed. By combing the model of control loops with that of the power stage, the closed-loop small-signal models of GFL- and GFM-MMCs have been developed [27]-[30], in which the frequency-coupling dynamics is characterized by using the multiple-input-multiple-output (MIMO) impedance matrix (IM). Yet, [27]-[29] focus on modeling the MMC only, whereas the stability analysis has not been performed. In [30], the stability study of the MMC connecting to the wind farm is carried out by considering the centered-diagonal element in the IM only, whereas non-zero frequency-coupling terms are ignored, which may lead to inaccurate stability predictions. The systematic stability analysis of MMCs that considering the frequency-coupling terms has not yet been thoroughly investigated in literatures, which also brings in challenges of formulating controller design guidelines for stabilizing the MMC system under different operating scenarios.

The internal dynamics of the MMC not only lead to the frequency-coupling nature of its power stage, but also brings in the 2^{nd}-order harmonic circulating current [31]. The circulating current suppression control (CCSC) is thus adopted to suppress the 2^{nd}-order harmonic circulating current [31]. The existing design guidelines for the CCSC

mainly consider its steady-state harmonic suppression capability, whereas its impact on system stability (as illustrated in Fig. 1.2 (b)) have been overlooked [31]-[32]. As a result, the zero-sequence circulating current (ZSCC) control is deemed as unnecessary in classical CCSCs, due to the absence of zero-sequence harmonics in the circulating current under the normal operation of MMCs [32]. Yet, recent studies show that the resonances might occur in the DC-link of the MMC without the ZSCC control [33]-[35]. Nevertheless, the work in [33]-[35] assume a strong ac grid without the grid impedance, and the stability impact of the ZSCC control when the MMC connecting to the weak ac grid is not addressed.

1.2.2. Transient Stability Analysis of VSCs

The VSCs might or might not have equilibrium points under large disturbances [36]. The LOS of VSCs is inevitable if there is no equilibrium point, but it may also take place even when there are equilibrium points. The transient stability of VSCs with equilibrium points are determined by their synchronization dynamics. Differing from SGs that can naturally synchronize with the power grid through its power-angle swing dynamics [1], the synchronization dynamics of VSCs are found to be dependent on their synchronization control loops, i.e., the APL for GFM-VSCs and the PLL for GFL-VSCs [10]-[11].

For GFM-VSCs, the simplest case is yielded when the VSC is controlled to mimic the dynamics of the SG, e.g., virtual synchronous generator (VSG) control [37]-[38]. In that case, the well-established methodology for analyzing the transient stability of SGs, e.g., equal area criterion (EAC), can be directly adopted [39]. Yet, there are other active power control alternatives for GFM-VSCs, e.g., the power synchronization control (PSC) [40]-[44] and the basic droop control [45], in which their APLs exhibit the first-order dynamics, and thus are different from the second-order swing dynamics of SGs. The design-oriented transient stability analysis of VSCs with the first-order APL has been hitherto unaddressed in literatures and thus worth investigating.

The PLL of the GFL-VSC features second-order synchronization dynamics, and hence, is identified to have the similar transient stability issue as SGs [36]. Meanwhile, there are stringent grid codes specifying the fault current injection profile of GFL-VSCs [46]. Existing solutions in literatures, e.g., freezing the PLL [47] or changing the active/reactive current profile during the fault [48]-[51], do enhance the transient stability of GFL-VSCs, but on the other hand pose new risks of violating the grid code. Therefore, the solution which can guarantee the transient stability of GFL-VSCs without violating the grid code is still demanded.

1.3. Project Objectives and Limitations

1.3.1. Project Objectives

To fill the void in the state of the art research, the objectives of this PhD project are defined as follows:

- Design-oriented small-signal stability analysis of the stand-alone operated MMC with GFM control

  This PhD project will develop the accurate small-signal model of the stand-alone operated MMC with GFM control, based on which, the impact of the ac voltage regulator on the IM of the MMC will be quantified, and a systematic stability analysis of the MMC considering its frequency coupling terms will also be performed. Finally, a design guideline of the ac voltage regulator to stabilize the MMC system will be given.

- Stability impact of the ZSCC control for the GFL-MMC under the weak ac grid

  The dynamic comparison of the GFL-MMC with and without the ZSCC control will be carried out in this PhD project, based on which, the stability impact of the ZSCC control will be revealed. Moreover, a parameter tuning guideline for the ZSCC controller to stabilize the MMC under the weak grid condition will also be given.

- Design-oriented transient stability analysis of GFM-VSCs with the PSC

  Taking the PSC as an example, the phase portrait is adopted in this PhD project to characterize the transient stability of VSCs with the first-order power angle control, and its superior transient stability performance over SGs with the second-order swing dynamics will also be highlighted.

- Design-oriented transient stability analysis of GFL-VSCs with the PLL

  The transient stability impact of the PLL on GFL-VSCs will be characterized in this PhD project. Moreover, the improved PLL scheme will also be proposed, which is able to guarantee the transient stability of GFL-VSCs without violating the grid code.

1.3.2. Project Limitations

This PhD project performs a design-oriented small-signal stability analysis of MMCs and transient stability analysis of VSCs. However, there are some limitations in this PhD project:

- Following the common practice in literatures [26]-[30], the arm-averaged model of the MMC is adopted in the PhD project as the basis for the small-signal modeling and stability analysis. However, the dynamic impact of the capacitor voltage balancing control and the switching action of the MMC cannot be reflected in the arm-averaged model [19]. Therefore, the developed small-signal model is only valid in the frequency range lower than the control frequency of the MMC (e.g. 10 kHz [7]). While the unstable operation of the MMC with the oscillation frequency close or higher than its control frequency is rarely reported in practice, it is still of interest from theoretical perspective to derive the accurate model of the MMC by considering all the control dynamics.
- The inner loops (voltage and current loops) are neglected when analyzing the transient stability of GFM- and GFL-VSCs, due to the generally decoupled timescale between outer loops (the power control loops and the PLL) and inner loops [18], [52]. Yet, this assumption does not hold for the high-power VSCs, in which the bandwidths of inner loops are constrained by the low switching frequency, and might not be sufficiently decoupled from that of outer loops [53]. Therefore, both inner and outer loops should be considered for analyzing the transient stability of high-power VSCs.
- Only the alternating-voltage control (AVC) is considered when analyzing the transient stability of the PSC-VSC, with which the magnitude of the terminal voltage can be controlled as a constant value [40]. Yet, there are other control alternatives, e.g., the constant reactive power control [40] or the Q-V droop control [45], with which the terminal voltage magnitude of the VSC is changed during the transient disturbances, and hence, the transient stability performance would be different. This issue has been partly addressed in our following work in [54], but more complete investigation is still needed.

1.4. Thesis Structure

Fig. 1.4 shows the structure of the PhD thesis. Chapter 1 introduces the background and motivation of the PhD project, after which its objectives and limitations are also discussed. The small-signal models of the GFM- and GFL-MMC are developed in Chapter 2 and Chapter 3, respectively, based on which, the dynamic impacts of the ac voltage control and the ZSCC control are characterized, and the controller design guidelines for stabilizing the MMC under different operating scenarios are also addressed. Chapter 4 analyzes the transient stability of the PSC-VSC, in which the dynamic impact of the first-order power-angle control is characterized by using the phase portrait. The same methodology is adopted to analyze the transient stability impact of the PLL in Chapter 5, and the improved PLL scheme is proposed to enhance the transient stability of the VSC. Chapter 6 concludes the findings of the PhD project.

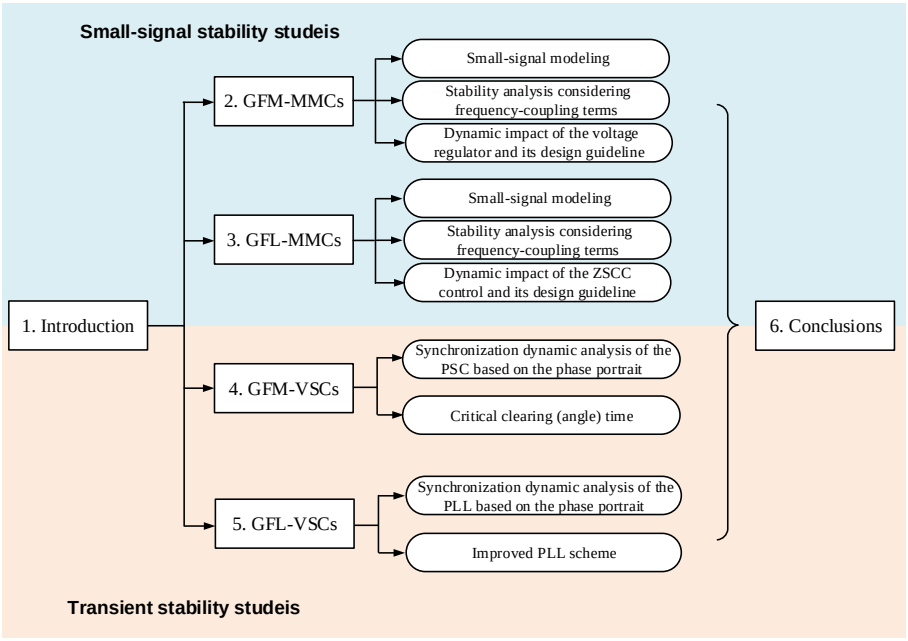

Figure 1.4. Thesis structure.

1.5. List of Publications

The relationship between the chapter number and published papers is given by Table 1.1.

Table 1.1. Relationship between the Chapter Number and Published Papers

Chapter No.	Related Publications
2	J1, C1
3	J2
4	J3, C2
5	J4, C3, C4

Journal Papers

J1. **H. Wu**, X. Wang, and Ł. Kocewiak, "Impedance-based stability analysis of voltage-controlled MMCs feeding linear AC systems," *IEEE J. Emerg. Sel. Topics Power Electron*., early access, 2019. DOI: 10.1109/JESTPE.2019.2911654.

J2. **H. Wu** and X. Wang, "Dynamic impact of zero-sequence circulating current on modular multilevel converters: complex valued AC impedance modeling and analysis," *IEEE J. Emerg. Sel. Topics Power Electron*., early access, 2019. DOI: 10.1109/JESTPE.2019.2951446.

J3. **H. Wu** and X. Wang, "Design-oriented transient stability analysis of grid-connected converters with power synchronization control," *IEEE Trans. Ind. Electron.*, vol. 66, no. 8, pp. 6473–6482, Aug. 2019.

J4. **H. Wu** and X. Wang, "Design-oriented transient stability analysis of PLL-synchronized voltage-source converters," *IEEE Trans. Power Electron.*, vol. 35, no. 4, pp. 3573 - 3589, Apr. 2020.

Conference Papers

C1. **H. Wu**, X. Wang, L. Kocewiak, and L. Harnefors, "AC impedance modeling of modular multilevel converters and two-level voltage-source converters: Similarities and differences," in *Proc. IEEE 19th Workshop Control. Model. Power Electron. (COMPEL)*, Jun. 2018, pp. 1–8.

C2. **H. Wu** and X. Wang, "Transient angle stability analysis of grid-connected converters with the first-order active power loop," in *Proc. IEEE Appl. Power Electron. Conf. Expo.*, Mar. 2018, pp. 3011–3016.

C3. **H. Wu** and X. Wang, "Transient stability impact of the phase-locked loop on grid-connected voltage source converters," in *Proc. IEEE Int. Power Electron. Conf. (IPEC-ECCE Asia)*, 2018, pp. 2673–2680.

C4. **H. Wu** and X. Wang, "An adaptive phase-locked loop for the transient stability enhancement of grid-connected voltage source converters," in *Proc. IEEE Energy Convers. Congr. Expo.*, 2018, pp. 5892–5898.

.

Chapter 2. Modeling and Stability Analysis of the Stand-alone Operated MMC with GFM Control

The content of this chapter is based on **J1 and C1**.

2.1. Background

With the increased penetration of modular multilevel converters (MMCs) in the electric power grids, dynamic interactions between MMCs, weak ac power grids and industrial loads are becoming more apparent. A number of incidents regard the resonance of MMC systems have recently been reported [4], [7]. Typically, the MMC can be operated either in the stand-alone mode or the grid-connected mode [55]. The stability of the stand-alone operated MMC with GFM control is the focus of this chapter, while the stability of the grid-connected MMC with GFL control will be addressed in Chapter 3.

As the precondition of the stability study, it is of vital importance to develop an accurate small-signal model of the MMC. Differing from two-/three-level voltage source converters (VSCs), whose small-signal model is already mature [15]-[18], the small-signal model of the MMC is much more complex due to its unique internal control dynamics, i.e., capacitor voltage variations [19]. The internal dynamics of the MMC will lead to the frequency coupling behavior at the ac terminal, which should be characterized by the multiple-input-multiple-output (MIMO) impedance matrix (IM) [26]-[30]. Although the small-signal modeling of the MMC has already been addressed in [26]-[30], the controller parametric impact on the IM of the MMC has not been explicitly revealed. Moreover, while the stability analysis has been carried out in [30], the impacts of frequency coupling terms of the IM of the MMC are ignored, which lead to inaccurate stability prediction. Therefore, how to design the voltage regulator to stabilize the stand-alone operated MMC system is still an open question.

To tackle this challenge, our work in [J1] presents the design-oriented small-signal stability analysis of the stand-alone operated MMC with GFM control, in which the impedance shaping effect of the voltage regulator is clearly revealed. The generalized Nyquist stability criterion (GNSC) is utilized to analyze the stability of the MMC with passive loads, based on which, the root cause of the sub-synchronous oscillation (SSO) is located, and the voltage controller design guideline for stabilizing the MMC system is also given. The main content of [J1] is summarized as follows.

2.2. Harmonic State Space Basics

The harmonic state space (HSS) method is adopted for developing the small-signal model of the MMC, and its modeling procedure is summarized as follows [56]:

By linearizing the nonlinear time-periodic (NTP) system, its linear time-periodic (LTP) small-signal representation can be obtained [56], which can be generally expressed as:

$$\begin{aligned} \frac{d\hat{x}(t)}{dt} &= A(t)\hat{x}(t) + B(t)\hat{u}(t) \\ \hat{y}(t) &= C(t)\hat{x}(t) + D(t)\hat{u}(t) \end{aligned} . \tag{2.1}$$

where $\hat{x}(t)$, $\hat{u}(t)$ and $\hat{y}(t)$ are the small-signal representation of state, input and output variables, respectively. $A(t)$, $B(t)$, $C(t)$ and $D(t)$ are time-periodic matrices, and their Fourier expansions are given by:

$$\begin{aligned} A(t) &= \sum_{h=-\infty}^{+\infty} A_h e^{jh\omega_0 t} \\ B(t) &= \sum_{h=-\infty}^{+\infty} B_h e^{jh\omega_0 t} \\ C(t) &= \sum_{h=-\infty}^{+\infty} C_h e^{jh\omega_0 t} \\ D(t) &= \sum_{h=-\infty}^{+\infty} D_h e^{jh\omega_0 t} \end{aligned} . \tag{2.2}$$

where ω_0 is the fundamental frequency, A_h, B_h, C_h and D_h are the corresponding hth Fourier coefficients of $A(t)$, $B(t)$, $C(t)$ and $D(t)$, respectively. Substituting (2.2) into (2.1), the s-domain representation of (2.1) can be expressed as [56]:

$$\begin{aligned} s\hat{\mathbf{x}} &= \mathbf{A}_{\mathbf{hss}}\hat{\mathbf{x}} + \mathbf{B}_{\mathbf{hss}}\hat{\mathbf{u}} \\ \hat{\mathbf{y}} &= \mathbf{C}_{\mathbf{hss}}\hat{\mathbf{x}} + \mathbf{D}_{\mathbf{hss}}\hat{\mathbf{u}} \end{aligned} . \tag{2.3}$$

$$\begin{aligned} \hat{\mathbf{x}} &= \begin{bmatrix} \dots & \hat{X}_{-h} & \dots & \hat{X}_{-1} & \hat{X}_0 & \hat{X}_1 & \dots & \hat{X}_h & \dots \end{bmatrix}^T \\ \hat{\mathbf{u}} &= \begin{bmatrix} \dots & \hat{U}_{-h} & \dots & \hat{U}_{-1} & \hat{U}_0 & \hat{U}_1 & \dots & \hat{U}_h & \dots \end{bmatrix}^T \\ \hat{\mathbf{y}} &= \begin{bmatrix} \dots & \hat{Y}_{-h} & \dots & \hat{Y}_{-1} & \hat{Y}_0 & \hat{Y}_1 & \dots & \hat{Y}_h & \dots \end{bmatrix}^T \end{aligned} . \tag{2.4}$$

$$\begin{aligned}\mathbf{A_{hss}} &= \mathbf{\Gamma}[A] - \mathbf{N} \\ \mathbf{B_{hss}} &= \mathbf{\Gamma}[B] \\ \mathbf{C_{hss}} &= \mathbf{\Gamma}[C] \\ \mathbf{D_{hss}} &= \mathbf{\Gamma}[D]\end{aligned} . \tag{2.5}$$

N is expressed as

$$\mathbf{N} = \mathrm{diag}[\ldots \quad -jh\omega_0\mathbf{I} \quad \ldots \quad -j\omega_0\mathbf{I} \quad \mathbf{I} \quad j\omega_0\mathbf{I} \quad \ldots \quad jh\omega_0\mathbf{I} \quad \ldots]. \tag{2.6}$$

where **I** is the identity matrix, **Γ** represents the Toeplitz matrix, which is defined as (using **Γ**[*A*] as the example)

$$\mathbf{\Gamma}[A] = \begin{bmatrix} \ldots & \ldots & \ldots & \ldots & \ldots & \ldots \\ \ldots & A_0 & A_{-1} & \ldots & A_{-h} & \ldots \\ \ldots & A_1 & A_0 & \ldots & A_{-h+1} & \ldots \\ \ldots & \ldots & \ldots & \ldots & \ldots & \ldots \\ \ldots & A_h & A_{h-1} & \ldots & A_0 & \ldots \\ \ldots & \ldots & \ldots & \ldots & \ldots & \ldots \end{bmatrix}. \tag{2.7}$$

It is known from (2.7) that the elements of $\mathbf{A_{hss}}$, $\mathbf{B_{hss}}$, $\mathbf{C_{hss}}$ and $\mathbf{D_{hss}}$ are time-invariant Fourier coefficients given by (2.2), and thus, (2.3) provides the linear time-invariant (LTI) representation of the LTP system, which facilitates the stability analysis by using the linear control theory. The dimensions of $\mathbf{A_{hss}}$, $\mathbf{B_{hss}}$, $\mathbf{C_{hss}}$ and $\mathbf{D_{hss}}$ are infinite in theory, but practically these matrices can be truncated by considering the major harmonic components [56].

2.3. Modeling of the MMC

Fig. 2.1 shows the single-line diagram of the GFM-MMC connecting to the inductive load, and the arm averaged model of its power stage is given in Fig. 2.2 [19]. L_{arm}, L_{load}, R_{arm} and R_{load} represent the inductance and resistance of the arm filter of the MMC and the passive load, respectively. Since the synchronization is not necessary for the stand-alone operated MMC, the power control loops are not used. Hence, only the ac voltage control and the circulating current suppression control (CCSC) are adopted for the GFM-MMC operated in the stand-alone mode [55]. Table 2.1 provides the definition of the variables used in the following analysis.

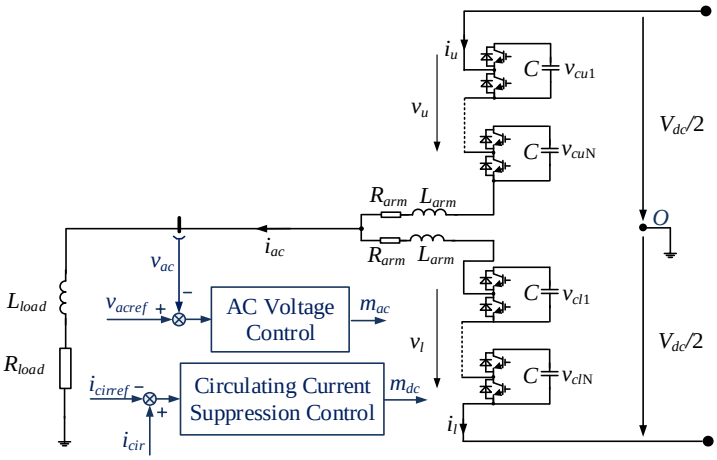

Figure 2.1. Circuit diagram of the voltage-controlled MMC powering the inductive load. Source: [J1].

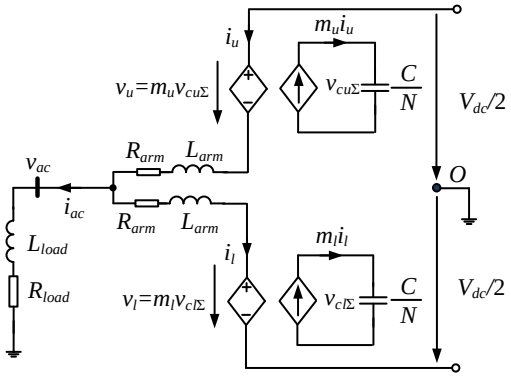

Figure 2.2. Arm averaged model of the MMC. Source: [J1].

Table 2.1. Definition of Variables.

SYMBOL	DESCRIPTION
v_u, v_l	Arm voltages for the upper and lower arms
i_u, i_l	Arm currents for the upper and lower arms
$v_{cu\Sigma}$, $v_{cl\Sigma}$	Sum of submodule capacitor voltages for the upper and lower arms
m_u, m_l	Control signals for the upper and lower arms
v_{ac}, i_{ac}	Output ac voltage and current, $i_{ac}= i_u-i_l$
i_{cir}	Circulating current, $i_{cir}=(i_u+i_l)/2$
$v_{c\Sigma}$, $v_{c\Delta}$	Sum and difference of the capacitor voltages of the upper and lower arms, $v_{c\Sigma}= v_{cu\Sigma}+v_{cl\Sigma}$, $v_{c\Delta}= v_{cu\Sigma}-v_{cl\Sigma}$
m_{ac}	Control signal generated from the ac voltage control loop, $m_{ac}= (m_l- m_u)/2$
m_{dc}	Control signal generated from the CCSC, $m_{dc}= m_u + m_l$

2.3.1. Modeling of the Power Stage

Based on Kirchhoff's law and Ohm's law, the NTP representation of the MMC can be formulated by means of differential equations, which are detailed in [J1]. Then, linearization is performed to obtain the small-signal LTP model of the MMC, which is given by:

$$\dot{\hat{\mathbf{x}}}(\mathbf{t}) = \mathbf{A}(\mathbf{t})\hat{\mathbf{x}}(\mathbf{t}) + \mathbf{B(t)}\hat{\mathbf{u}}(\mathbf{t}) . \tag{2.8}$$

where

$$\begin{aligned} \hat{\mathbf{x}}(\mathbf{t}) &= \begin{bmatrix} \hat{i}_{ac}(t) & \hat{i}_{cir}(t) & \hat{v}_{c\Sigma}(t) & \hat{v}_{c\Delta}(t) \end{bmatrix} \\ \hat{\mathbf{u}}(\mathbf{t}) &= \begin{bmatrix} \hat{m}_{ac}(t) & \hat{m}_{dc}(t) & \hat{v}_{ac}(t) & \hat{v}_{dc}(t) \end{bmatrix} \end{aligned} . \tag{2.9}$$

$$\mathbf{A}(\mathbf{t}) = \begin{bmatrix} -\frac{R_{arm}}{L_{arm}} & 0 & \frac{M_{ac}(t)}{L_{arm}} & -\frac{M_{dc}(t)}{2L_{arm}} \\ 0 & -\frac{R_{arm}}{L_{arm}} & -\frac{M_{dc}(t)}{4L_{arm}} & \frac{M_{ac}(t)}{2L_{arm}} \\ -\frac{N}{C}M_{ac}(t) & \frac{N}{C}M_{dc}(t) & 0 & 0 \\ \frac{N}{2C}M_{dc}(t) & -\frac{2N}{C}M_{ac}(t) & 0 & 0 \end{bmatrix} . \tag{2.10}$$

$$\mathbf{B}(\mathbf{t})=\begin{bmatrix} \frac{V_{c\Sigma}(t)}{L_{arm}} & -\frac{V_{c\Delta}(t)}{2L_{arm}} & -\frac{2}{L_{arm}} & 0 \\ \frac{V_{c\Delta}(t)}{2L_{arm}} & -\frac{V_{c\Sigma}(t)}{4L_{arm}} & 0 & \frac{1}{2L_{arm}} \\ -\frac{N}{C}I_{ac}(t) & \frac{N}{C}I_{cir}(t) & 0 & 0 \\ -\frac{2N}{C}I_{cir}(t) & \frac{N}{2C}I_{ac}(t) & 0 & 0 \end{bmatrix}. \tag{2.11}$$

Then, the HSS model of the MMC is derived by following the procedure in 2.2, and is given by

$$s\hat{\mathbf{x}}=\mathbf{A}_{\mathbf{hss}}\hat{\mathbf{x}}+\mathbf{B}_{\mathbf{hss}}\hat{\mathbf{u}}. \tag{2.12}$$

$$\begin{aligned} \hat{\mathbf{x}} &= \begin{bmatrix} \dots & \hat{X}_{-h} & \dots & \hat{X}_{-1} & \hat{X}_0 & \hat{X}_1 & \dots & \hat{X}_h & \dots \end{bmatrix}^T \\ \hat{X}_h &= \begin{bmatrix} \hat{i}_{ac}(s+jh\omega_0) & \hat{i}_{cir}(s+jh\omega_0) & \hat{v}_{c\Sigma}(s+jh\omega_0) & \hat{v}_{c\Delta}(s+jh\omega_0) \end{bmatrix}^T \end{aligned}. \tag{2.13}$$

$$\begin{aligned} \hat{\mathbf{u}} &= \begin{bmatrix} \dots & \hat{U}_{-h} & \dots & \hat{U}_{-1} & \hat{U}_0 & \hat{U}_1 & \dots & \hat{U}_h & \dots \end{bmatrix}^T \\ \hat{U}_h &= \begin{bmatrix} \hat{m}_{ac}(s+jh\omega_0) & \hat{m}_{dc}(s+jh\omega_0) & \hat{v}_{ac}(s+jh\omega_0) & \hat{v}_{dc}(s+jh\omega_0) \end{bmatrix}^T \end{aligned}. \tag{2.14}$$

where $\mathbf{A}_{\mathbf{hss}}$ and $\mathbf{B}_{\mathbf{hss}}$ are defined in (2.5).

2.3.2. Modeling of the Control Loops

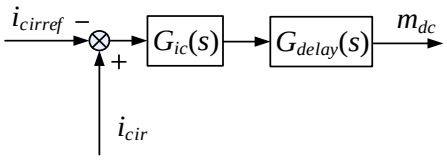

Figure 2.3. Block diagram of the CCSC. Source: [J1].

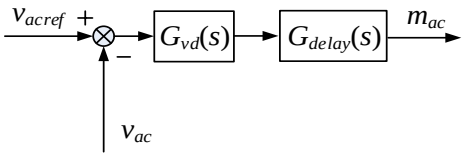

Figure 2.4. Block diagram of the ac voltage control loop. Source: [J1].

Fig. 2.3 and 2.4 show the block diagrams of the CCSC and the ac voltage control, respectively. Considering $\hat{i}_{cirref}=0$ and $\hat{v}_{acref}=0$, $\hat{m}_{ac}$ and $\hat{m}_{dc}$ can be expressed as

$$\hat{m}_{ac}\left(s+jh\omega_0\right)=-G_{vd}\left(s+jh\omega_0\right)G_{delay}\left(s+jh\omega_0\right)\hat{v}_{ac}\left(s+jh\omega_0\right). \tag{2.15}$$

$$\hat{m}_{dc}\left(s+jh\omega_0\right)=G_{ic}\left(s+jh\omega_0\right)G_{delay}\left(s+jh\omega_0\right)\hat{i}_{cir}\left(s+jh\omega_0\right). \tag{2.16}$$

where $G_{delay}(s)$ represents the time delay in the control loop. $G_{ic}(s)$ and $G_{vd}(s)$ are the circulating current regulator and the ac voltage regulator, respectively. The proportional resonant (PR) regulators with the resonant frequencies fixed at $2\omega_0$ and ω_0 are used for $G_{ic}(s)$ and $G_{vd}(s)$, respectively, which are expressed as

$$G_{ic}\left(s\right)=K_{Pic}+\frac{2K_{Ric}\omega_i s}{s^2+2\omega_i s+\left(2\omega_0\right)^2}. \tag{2.17}$$

$$G_{vd}\left(s\right)=K_{Pvd}+\frac{2K_{Rvd}\omega_i s}{s^2+2\omega_i s+\omega_0^2} \tag{2.18}$$

2.4. Impedance Calculation

Eq. (2.12) can be rewritten as

$$\hat{\mathbf{x}}=\left(\mathbf{sI}-\mathbf{A}_{\mathbf{hss}}\right)^{-1}\mathbf{B}_{\mathbf{hss}}\hat{\mathbf{u}}=\mathbf{H}_{\mathbf{tfhss}}\hat{\mathbf{u}}. \tag{2.19}$$

Focusing on the relationship between $\hat{i}_{ac}\left(s+jh\omega_0\right)$ and $\hat{v}_{ac}\left(s+jh\omega_0\right)$, the admittance matrix is the submatrix of $\mathbf{H}_{\mathbf{tfhss}}$, which is given by

$$\hat{\mathbf{i}}_{\mathbf{ac}} = \mathbf{Y}_{\mathbf{MMC}}\hat{\mathbf{v}}_{\mathbf{ac}}$$

$$\mathbf{Y}_{\mathbf{MMC}} = \begin{bmatrix} \ddots & \vdots & & \vdots & \iddots \\ & Y_0(s-j\omega_0) & Y_{-1}(s) & Y_{-2}(s+j\omega_0) & \\ \cdots & Y_1(s-j\omega_0) & Y_0(s) & Y_{-1}(s+j\omega_0) & \cdots \\ & Y_2(s-j\omega_0) & Y_1(s) & Y_0(s+j\omega_0) & \\ \iddots & \vdots & & \vdots & \ddots \end{bmatrix}. \tag{2.20}$$

$$\hat{\mathbf{i}}_{\mathbf{ac}} = \begin{bmatrix} \cdots & \hat{i}_{ac}(s-j\omega_0) & \hat{i}_{ac}(s) & \hat{i}_{ac}(s+j\omega_0) & \cdots \end{bmatrix}^T$$

$$\hat{\mathbf{v}}_{\mathbf{ac}} = \begin{bmatrix} \cdots & \hat{v}_{ac}(s-j\omega_0) & \hat{v}_{ac}(s) & \hat{v}_{ac}(s+j\omega_0) & \cdots \end{bmatrix}^T$$

$$\mathbf{Z}_{\mathbf{MMC}} = \mathbf{Y}_{\mathbf{MMC}}^{-1} = \begin{bmatrix} \ddots & \vdots & & \vdots & \iddots \\ & Z_0(s-j\omega_0) & Z_{-1}(s) & Z_{-2}(s+j\omega_0) & \\ \cdots & Z_1(s-j\omega_0) & Z_0(s) & Z_{-1}(s+j\omega_0) & \cdots \\ & Z_2(s-j\omega_0) & Z_1(s) & Z_0(s+j\omega_0) & \\ \iddots & \vdots & & \vdots & \ddots \end{bmatrix}. \tag{2.21}$$

The frequency coupling dynamics of the power stage of the MMC can be clearly observed from (2.20) and (2.21), which are dictated by the off-diagonal elements of the matrices. In the following, the centered-diagonal element of the IM, i.e., $Z_0(s)$, is defined as centered-diagonal impedance, while the off-diagonal elements are defined as frequency-coupled impedances.

2.4.1. AC-side Open-loop Impedance

Only the CCSC is considered when deriving the ac-side open-loop IM of the MMC, and thus, $\mathbf{Z}_{\mathbf{MMC}}$ can be calculated by substituting $\hat{m}_{ac}(s+jh\omega_0)=0$ and (2.16) into (2.19).

Fig. 2.5 shows the Bode diagram of the centered-diagonal impedance $Z_{open0}(s)$. It can be seen that the measurement results given by cross marks "x" match closely with the theoretical analysis, which verifies the correctness of the mathematical modeling. Moreover, the calculated $Z_{open0}(s)$ considering up to fundamental frequency (h=1) is similar to that considering up to 2nd harmonics (h=2). It is because the 2nd harmonic in the circulating current is effectively suppressed by the CCSC, and thus, it can be neglected during the modeling procedure.

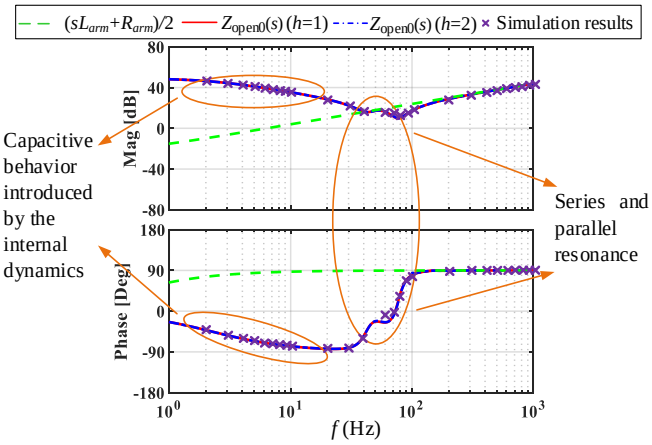

Figure 2.5. Impedance plot of $Z_0(s)$ with open-loop control. Source: [J1].

It is worth mentioning that without considering the internal dynamics of the MMC, its open-loop impedance is merely the filter inductance, i.e., $(sL_{arm}+R_{arm})/2$ [C1], [J1]. Yet, it can be clearly observed from Fig 2.5 that the internal dynamics of the MMC leads to the capacitive behavior of $Z_{open0}(s)$ in the low-frequency range, which is significantly different from the inductive behavior of the filter impedance. On the other hand, the high-frequency (> 200 Hz) impact of the internal dynamics is negligible, as dictated by the close match between the filter impedance and $Z_{open0}(s)$ in the high-frequency range. This can be understood from the filtering characteristic of the capacitor, which leads to the smaller high-frequency capacitor voltage ripple and the reduced high-frequency dynamic impact.

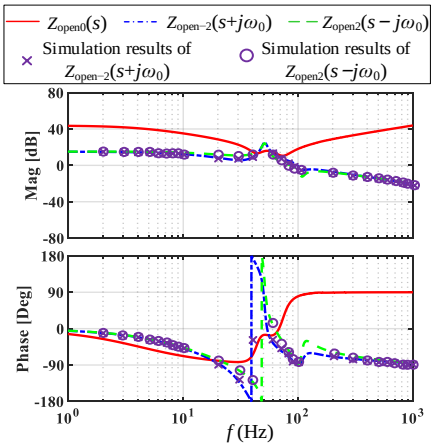

Figure 2.6. Bode diagram of the centered-diagonal and frequency-coupled impedances of the MMC with the open-loop control. Source: [J1].

For the frequency-coupled impedances, it turns out that $Z_{open1}(s-j\omega_0) = Z_{open1}(s) = Z_{open-1}(s) = Z_{open-1}(s+ j\omega_0)=0$ [J1], while the Bode diagrams of $Z_{open2}(s-j\omega_0)$ and $Z_{open-2}(s+j\omega_0)$ are given in Fig. 2.6. It can be seen that the magnitudes of $Z_{open2}(s-j\omega_0)$ and $Z_{open-2}(s+j\omega_0)$ are much lower than that of $Z_{open0}(s)$ in the high-frequency range (> 200 Hz), and thus, their impacts on the high-frequency dynamics of the MMC can also be neglected.

2.4.2. AC-side Closed-loop Impedance

Both the ac voltage control loop and the CCSC are considered for deriving the ac-side closed-loop IM of the MMC. Therefore, $\mathbf{Z_{MMC}}$ can be calculated by substituting (2.15) and (2.16) into (2.19).

It is demonstrated in [J1] that the dynamic impact of $G_{vd}(s)$ on the centered-diagonal impedance of the MMC is same as that of the two-/three-level VSC, which is:

$$Z_{close0}(s) = \frac{Z_{open0}(s)}{1+V_{dc}G_{vd}(s)G_{delay}(s)}. \tag{2.22}$$

This conclusion provides insight for the design of $G_{vd}(s)$. On the other hand, the impact of $G_{vd}(s)$ on the frequency-coupled impedances is much more complex, which is detailed in [J1].

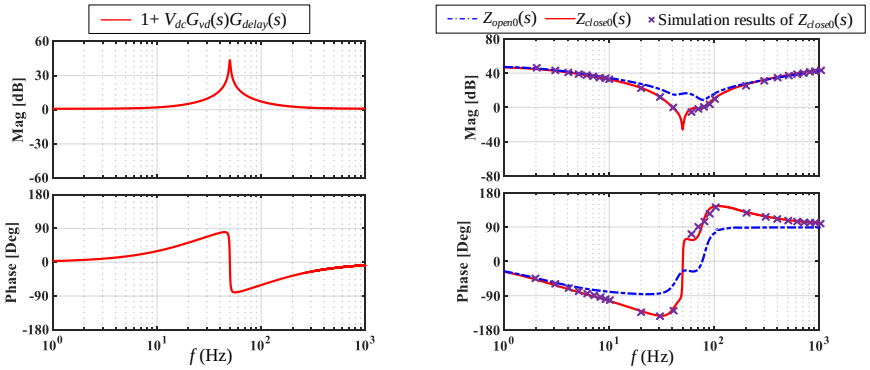

(a) (b)

Figure 2.7. (a) Bode diagram of $1+ V_{dc}G_{vd}(s)G_{delay}(s)$. (b) Bode diagram of $Z_{open0}(s)$ and $Z_{close0}(s)$. Source: [J1].

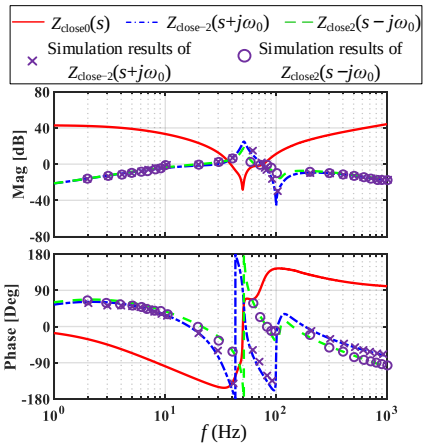

Figure 2.8. Bode diagram of the centered-diagonal and frequency-coupled impedances of the MMC with closed-loop control. Source: [J1].

Fig. 2.7 shows the Bode diagrams of 1+ $V_{dc}G_{vd}(s)G_{delay}(s)$, $Z_{open0}(s)$ and $Z_{close0}(s)$, respectively. It can be seen that $Z_{close0}(s)$ is inversely proportional to 1+ $V_{dc}G_{vd}(s)G_{delay}(s)$, as dictated by (2.22).

Fig. 2.8 shows the Bode diagram of the frequency-coupled impedances of the closed-loop controlled MMC. Similar to the open-loop controlled MMC, these frequency-coupled impedances should be considered in the low-frequency stability analysis, but can be neglected in the high-frequency stability analysis.

2.5. Stability Criterion

As the frequency-coupled impedances have significant impacts on the low-frequency dynamics of the MMC, the GNSC should be used for the low-frequency stability study [57]. The stability of the unloaded MMC should be guaranteed before analyzing its interaction with the load [58]. Therefore, there are no right-half-plane (RHP) poles in $\mathbf{Z_{MMC}}$ [58]. In that case, the interconnected system given in Fig. 2.1 will be stable if and only if the eigen-loci of the return-ratio matrix $\mathbf{Z_{MMC}Y_{load}}$ do not encircle the critical point (−1+j0) [57].

The eigenvalues of $\mathbf{Z_{MMC}Y_{load}}$ is calculated as

$$\det\left(\lambda\mathbf{I}-\mathbf{Z}_{\mathbf{MMC}}\mathbf{Y}_{\mathbf{Load}}\right)=0\,. \tag{2.23}$$

Only the passive linear load is considered in this work, and thus, $\mathbf{Y_{load}}$ is expressed as

$$\mathbf{Y_{load}} = \mathrm{diag}\left[Y_{load}(s - j\omega_0) \quad Y_{load}(s) \quad Y_{load}(s + j\omega_0) \right]. \tag{2.24}$$

Substituting (2.24) into (2.23), three eigenvalues are expressed as

$$\lambda_1 = Z_0(s) Y_{load}(s). \tag{2.25}$$

$$\lambda_2 = a(s) - b(s). \tag{2.26}$$

$$\lambda_3 = a(s) + b(s). \tag{2.27}$$

where

$$a(s) = \frac{Z_0(s - j\omega_0) Y_{Load}(s - j\omega_0) + Z_0(s + j\omega_0) Y_{Load}(s + j\omega_0)}{2}. \tag{2.28}$$

$$b(s) = \frac{\sqrt{\left[Z_0(s - j\omega_0) Y_{Load}(s - j\omega_0) + Z_0(s + j\omega_0) Y_{Load}(s + j\omega_0) \right]^2 - 4 Y_{Load}(s - j\omega_0) Y_{Load}(s + j\omega_0) \begin{bmatrix} Z_0(s - j\omega_0) Z_0(s + j\omega_0) \\ -Z_{-2}(s + j\omega_0) Z_2(s - j\omega_0) \end{bmatrix}}}{2}. \tag{2.29}$$

It is known from (2.25) that one eigenvalue is equal to the impedance ratio between the centered-diagonal impedance of the MMC and the load impedance. Therefore, the stability analysis can be carried out by first checking whether this impedance ratio satisfies the single-input-single-output (SISO) Nyquist stability criterion. If not, the system is unstable and it is unnecessary to check other two eigenvalues, which avoids the complex eigenvalue calculation based on (2.23). Fig. 2.9 shows the overall flow chart for the stability analysis, which is simpler and more straightforward compared with calculating eigenvalues directly.

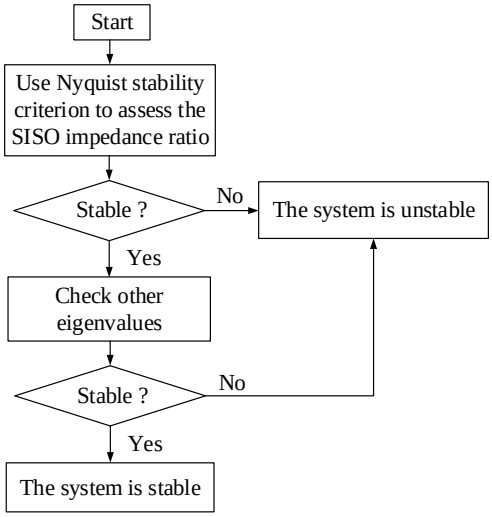

Figure 2.9. Flow chart of the stability assessment of the MMC interacts with the linear system. Source: [J1].

2.6. Case Studies

In this part, case studies are carried out for the GFM-MMC with PR voltage regulator powering the inductive load. Following the procedure given in Fig. 2.9, the impedance ratio $Z_{close0}(s)Y_{load}(s)$ is first checked. The used controller parameters are $K_{Pvd}=5\cdot10^{-7}$, $K_{Rvd}=7.5\cdot10^{-4}$, $\omega_i=\pi$, and the main circuit parameters are given in Table 2.2.

Table 2.2. Main Circuit Parameters of the MMC. Source: [J1]

SYMBOL	DESCRIPTION	VALUE
V_{grms}	RMS value of grid voltage (line to line)	100 kV
f_g	Grid frequency	50 Hz
P_o	Rated output power	100 MW
V_{dc}	DC side voltage	±100 kV
L_{arm}	Arm inductance	45 mH
R_{arm}	Arm resistance	0.15 Ω
C_{sm}	Capacitance of the submodule	3.3 mF
N	Number of the submodule each arm	100
L_{load}	Load inductance	318 mH

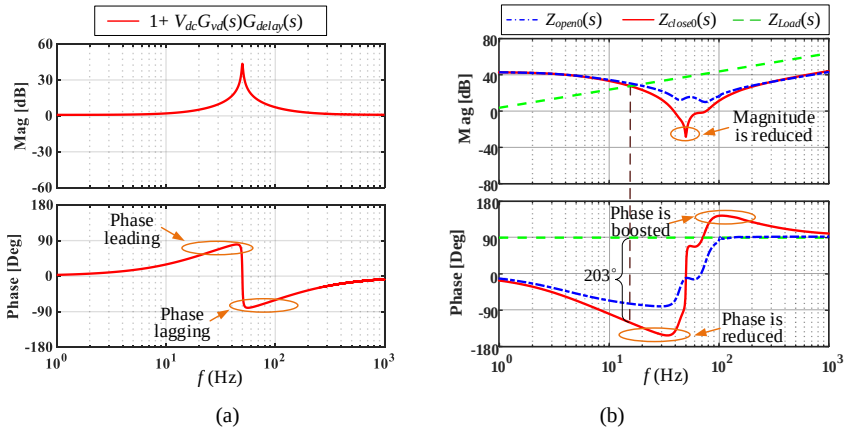

Figure 2.10. Bode diagram of the MMC with PR regulator. (a) Bode diagram of 1+ $V_{dc}G_{vd}(s)G_{delay}(s)$. (b) Bode diagram of $Z_{open0}(s)$, $Z_{close0}(s)$ and $Z_{Load}(s)$. Source: [J1].

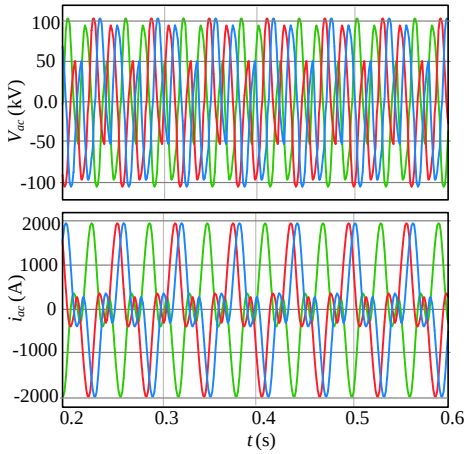

Figure 2.11. Simulation result of the MMC powering the inductive load with PR regulator. Source: [J1].

Fig. 2.10 shows the Bode diagram of 1+ $V_{dc}G_{vd}(s)G_{delay}(s)$, $Z_{open0}(s)$, $Z_{close0}(s)$ and $Z_{Load}(s)$, respectively. It can be seen that $Z_{close0}(s)$ exhibits a capacitance + negative resistance in the low-frequency range, due to the capacitive behavior of $Z_{open0}(s)$ and the phase leading effect of the PR regulator [J1], which leads to the phase difference between $Z_{close0}(s)$ and $Z_{Load}(s)$ to be higher than 180° at their magnitude intersection point. Therefore, the system is unstable and the check of other two eigenvalues is unnecessary, as verified by the time-domain simulation given by Fig. 2.11.

In order to guarantee the system stability, $G_{vd}(s)$ should be re-designed either to reduce the magnitude of $Z_{close0}(s)$ to avoid the magnitude intersection with $Z_{Load}(s)$, or to boost the phase of $Z_{close0}(s)$ to minimize its phase difference with $Z_{Load}(s)$ at their magnitude

intersection point. The prior method is adopted in this work. As $G_{vd}(s)$ appears at the denominator of (2.22), the magnitude of $Z_{close0}(s)$ can be reduced by increasing the gain of $G_{vd}(s)$. This can be achieved by adding an integrator to the original PR regulator, which leads to a PIR regulator, i.e.,

$$G_{vd}(s) = K_{Pvd} + \frac{K_{ivd}}{s} + \frac{2K_{Rvd}\omega_i s}{s^2 + 2\omega_i s + \omega_0^2}. \tag{2.30}$$

Fig. 2.12 shows the Bode diagram of $1+ V_{dc}G_{vd}(s)G_{delay}(s)$, $Z_{open0}(s)$, $Z_{close0}(s)$ and $Z_{Load}(s)$ with the PIR regulator, respectively. It can be seen that the magnitude intersection of $Z_{close0}(s)$ and $Z_{Load}(s)$ is avoided, and thus the SISO Nyquist stability criterion is met. In this case, other eigenvalues should also be checked to assess the system stability, as shown in Fig. 2.13. It can be seen that there are no eigen-loci encircling the critical point (−1+j0), indicating the stable operation of the system. This theoretical finding is further justified by time-domain simulation results given in Fig. 2.14.

More detailed discussions and case studies can be found in [J1].

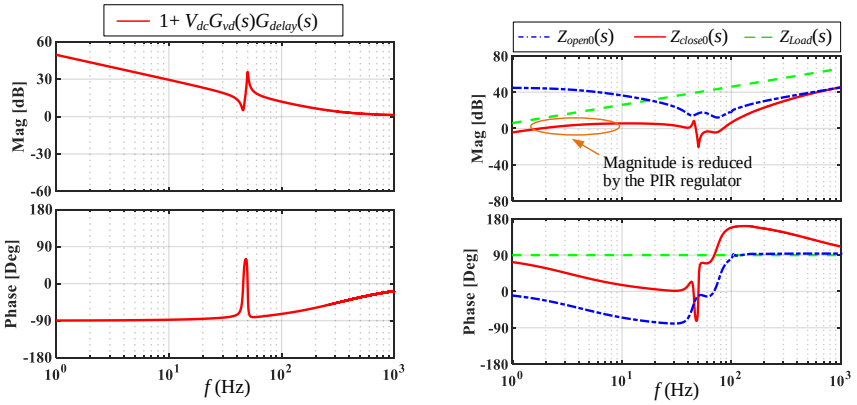

(a) (b)

Figure 2.12. Bode diagram of the MMC with the PIR regulator. (a) Bode diagram of $1+ V_{dc}G_{vd}(s)G_{delay}(s)$. (b) Bode diagram of $Z_{open0}(s)$, $Z_{close0}(s)$ and $Z_{Load}(s)$. Source: [J1].

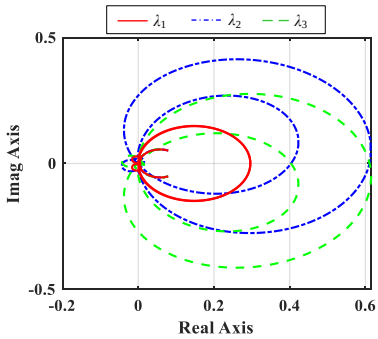

Figure 2.13. Nyquist diagram of eigen-loci of $\mathbf{Z}_{\mathbf{MMC}}\mathbf{Y}_{\mathbf{load}}$ with the PIR regulator. Source: [J1]

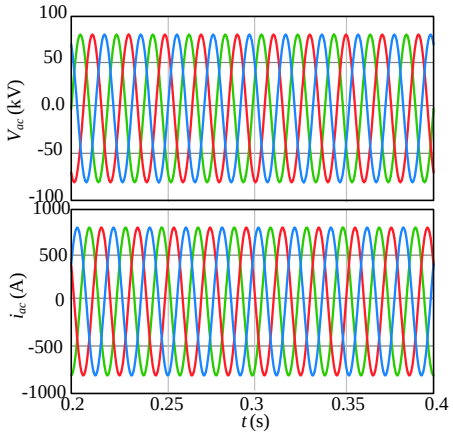

Figure 2.14. Simulation result of the MMC powering the inductive load with the PIR regulator. Source: [J1]

2.7. Summary

This chapter develops the small-signal model of the MMC with open-loop control and voltage-mode control, in which the impact of internal dynamics on the IM of the MMC is quantified. Stability analysis for the MMC with inductive loads are carried out based on the GNSC, and the major findings are:

- One eigenvalue of the return-ratio matrix is equal to impedance ratio between the centered-diagonal impedance of the MMC and the load impedance, and thus, this impedance ratio can be checked first by using the SISO Nyquist stability criterion.

- The MMC with the PR regulator introduces a capacitive plus negative damping behavior of $Z_{close0}(s)$ in the low-frequency range, which is the root cause to destabilize the MMC when connecting to the inductive load.
- The PIR regulator is used to stabilize the system.

All the theoretical findings are verified by time-domain simulations.

Chapter 3. Modeling and Stability Analysis of the GFL-MMC

The content of this chapter is based on **J2**.

3.1. Background

The circulating current suppression control (CCSC) is one of the basic control loops of the MMC [31], which is initially developed to suppress the 2nd-order harmonic in the circulating current. Detailed analysis have proven that this 2nd-order harmonic circulating current is the negative sequence component under the balanced power grid, whereas there is no zero-sequence circulating current (ZSCC) harmonics [32]. Therefore, the ZSCC control is deemed as unnecessary from the harmonic suppression perspective. Hence, there is no dedicated ZSCC control in the classical CCSC [31]. Yet, recent studies have found out that the ZSCC control has a significant impact on the stability of the MMC system. In [33]-[35], it is revealed that without the ZSCC control, the oscillation in the DC-link of the MMC can be easily triggered when it is connected with resonant DC cables. Nevertheless, a strong ac grid without grid impedance is assumed in these studies [33]-[35]. Hence, the stability impact of the ZSCC control when the MMC connects to the weak ac grid is still not clear.

To tackle this challenge, our work in [J2] develops the complete small-signal model of the GFL-MMC. Differing from the real-vector based model in [26]-[30]. The model in [J2] is represented by complex vectors, in which the ZSCC control dynamics can be directly captured. The ac-side single-input-single-output (SISO) equivalent impedance of the MMC is derived, based on which, the stability of the MMC with/without the ZSCC control is compared. Time-domain simulations are given to verify the theoretical analysis. The main content of [J2] is summarized as follows.

3.2. Modeling of the MMC

Fig. 3.1(a) shows the circuit diagram of the grid-connected MMC, while its arm-averaged model is given in Fig. 3.1 (b). All variables used in this chapter are defined in Table 2.1.

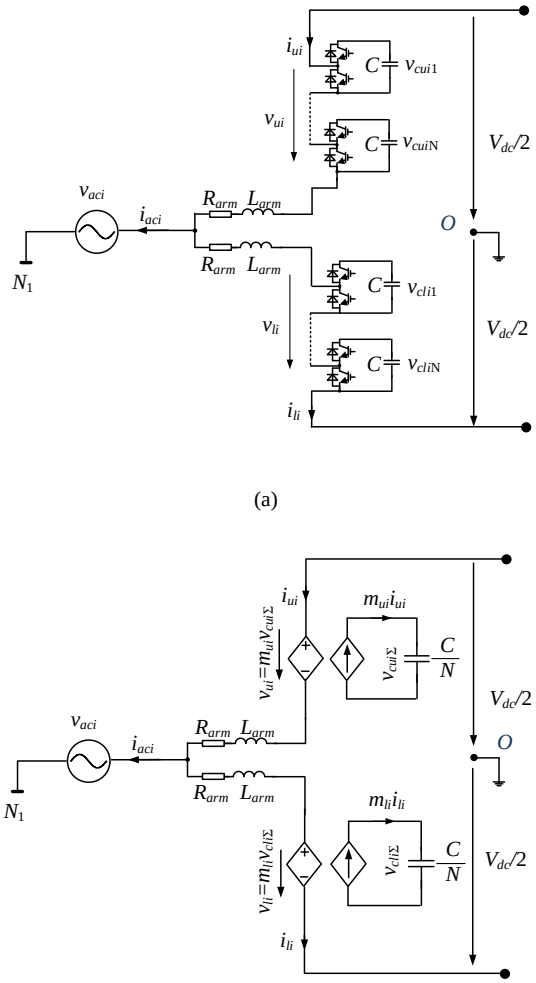

Figure 3.1. Single-phase diagram of the three-phase-three-wire grid-connected MMC. (a) Detailed circuit model. (b) Arm averaged model. Source: [J2].

3.2.1. Modeling of the Power Stage

Following the same procedure given by Section 2.3.1, the linear time periodic (LTP) small-signal model of the power stage of the MMC can be derived, which is given by

$$\dot{\hat{\mathbf{x}}}_{\mathbf{abc}}(\mathbf{t}) = \mathbf{A}_{\mathbf{abc}}(\mathbf{t})\hat{\mathbf{x}}_{\mathbf{abc}}(\mathbf{t}) + \mathbf{B}_{\mathbf{abc}}(\mathbf{t})\hat{\mathbf{u}}_{\mathbf{abc}}(\mathbf{t}) . \tag{3.1}$$

where

$$\begin{aligned} \hat{\mathbf{x}}_{\mathbf{abc}}(\mathbf{t}) &= \left[\hat{i}_{acabc}(t),\ \hat{i}_{cirabc}(t),\ \hat{v}_{c\sum abc}(t),\ \hat{v}_{c\Delta abc}(t)\right]^T \\ \hat{\mathbf{u}}_{\mathbf{abc}}(\mathbf{t}) &= \left[\hat{m}_{acabc}(t),\ \hat{m}_{dcabc}(t),\ \hat{v}_{acabc}(t),\ \hat{v}_{dcabc}(t)\right]^T \end{aligned} . \tag{3.2}$$

and $\mathbf{A_{abc}(t)}$ and $\mathbf{B_{abc}(t)}$ are given by (A.1) and (A.2) in [J2].

It is noted that (3.1) is represented by real vectors (*abc* three phase variables), and thus the ZSCC is not directly reflected in this model. In order to capture the ZSCC control impact, (3.1) can be equivalently transformed to the complex-vector representation by using the following transformation matrix, i.e.,

$$\mathbf{P} = \mathrm{diag}\left[T_1T_2,\ T_1T_2,\ T_1T_2,\ T_1T_2\right] . \tag{3.3}$$

where

$$\begin{bmatrix} x_{\alpha\beta+} \\ x_{\alpha\beta-} \\ x_{\alpha\beta 0} \end{bmatrix} = T_1 \begin{bmatrix} x_\alpha \\ x_\beta \\ x_0 \end{bmatrix} = T_1T_2 \begin{bmatrix} x_a \\ x_b \\ x_c \end{bmatrix} . \tag{3.4}$$

$$T_1 = \begin{pmatrix} 1 & j & \\ 1 & -j & \\ & & 1 \end{pmatrix} \qquad T_2 = \begin{pmatrix} \frac{2}{3} & -\frac{1}{3} & -\frac{1}{3} \\ 0 & \frac{\sqrt{3}}{3} & -\frac{\sqrt{3}}{3} \\ \frac{1}{3} & \frac{1}{3} & \frac{1}{3} \end{pmatrix} . \tag{3.5}$$

which leads to

$$\begin{aligned} &\mathbf{P^{-1}}\dot{\hat{\mathbf{x}}}_{\boldsymbol{\alpha\beta}+\mathbf{-0}}(\mathbf{t}) = \mathbf{A}_{\mathbf{abc}}(\mathbf{t})\left[\mathbf{P^{-1}}\hat{\mathbf{x}}_{\boldsymbol{\alpha\beta}+\mathbf{-0}}(\mathbf{t})\right] + \mathbf{B}_{\mathbf{abc}}(\mathbf{t})\left[\mathbf{P^{-1}}\hat{\mathbf{u}}_{\boldsymbol{\alpha\beta}+\mathbf{-0}}(\mathbf{t})\right] \Leftrightarrow \\ &\dot{\hat{\mathbf{x}}}_{\boldsymbol{\alpha\beta}+\mathbf{-0}}(\mathbf{t}) = \left[\mathbf{P}\mathbf{A}_{\mathbf{abc}}(\mathbf{t})\mathbf{P^{-1}}\right]\hat{\mathbf{x}}_{\boldsymbol{\alpha\beta}+\mathbf{-0}}(\mathbf{t}) + \left[\mathbf{P}\mathbf{B}_{\mathbf{abc}}(\mathbf{t})\mathbf{P^{-1}}\right]\hat{\mathbf{u}}_{\boldsymbol{\alpha\beta}+\mathbf{-0}}(\mathbf{t}) \end{aligned} . \tag{3.6}$$

Then, following the procedure described in Section 2.2, the frequency-domain representation of (3.6) can be derived by using the harmonic state space (HSS) method, which is given by

$$s\hat{\mathbf{x}}_{\mathbf{\alpha\beta+-0}} = \mathbf{A}_{\mathbf{hss\alpha\beta+-0}}\hat{\mathbf{x}}_{\mathbf{\alpha\beta+-0}} + \mathbf{B}_{\mathbf{hss\alpha\beta+-0}}\hat{\mathbf{u}}_{\mathbf{\alpha\beta+-0}} \,. \tag{3.7}$$

$$\hat{\mathbf{x}}_{\mathbf{\alpha\beta+-0}} = \begin{bmatrix} \hat{X}_{-h} \\ \vdots \\ \hat{X}_{-1} \\ \hat{X}_{0} \\ \hat{X}_{1} \\ \vdots \\ \hat{X}_{h} \end{bmatrix}, \quad \hat{X}_h = \begin{bmatrix} \hat{i}_{ac\alpha\beta+-0}(s+jh\omega_0) \\ \hat{i}_{cir\alpha\beta+-0}(s+jh\omega_0) \\ \hat{v}_{c\sum\alpha\beta+-0}(s+jh\omega_0) \\ \hat{v}_{c\Delta\alpha\beta+-0}(s+jh\omega_0) \end{bmatrix}. \tag{3.8}$$

$$\hat{\mathbf{u}}_{\mathbf{\alpha\beta+-0}} = \begin{bmatrix} \hat{U}_{-h} \\ \vdots \\ \hat{U}_{-1} \\ \hat{U}_{0} \\ \hat{U}_{1} \\ \vdots \\ \hat{U}_{h} \end{bmatrix}, \quad \hat{U}_h = \begin{bmatrix} \hat{m}_{ac\alpha\beta+-0}(s+jh\omega_0) \\ \hat{m}_{dc\alpha\beta+-0}(s+jh\omega_0) \\ \hat{v}_{ac\alpha\beta+-0}(s+jh\omega_0) \\ \hat{v}_{dc\alpha\beta+-0}(s+jh\omega_0) \end{bmatrix}. \tag{3.9}$$

$$\mathbf{A}_{\mathbf{hss\alpha\beta+-0}} = \mathbf{\Gamma}\left[\mathbf{P}\mathbf{A}_{\mathbf{abc}}(\mathbf{t})\mathbf{P}^{-1}\right] - \mathbf{N} \,. \tag{3.10}$$

$$\mathbf{B}_{\mathbf{hss\alpha\beta+-0}} = \mathbf{\Gamma}\left[\mathbf{P}\mathbf{B}_{\mathbf{abc}}(\mathbf{t})\mathbf{P}^{-1}\right] . \tag{3.11}$$

3.2.2. Modeling of the Control loop

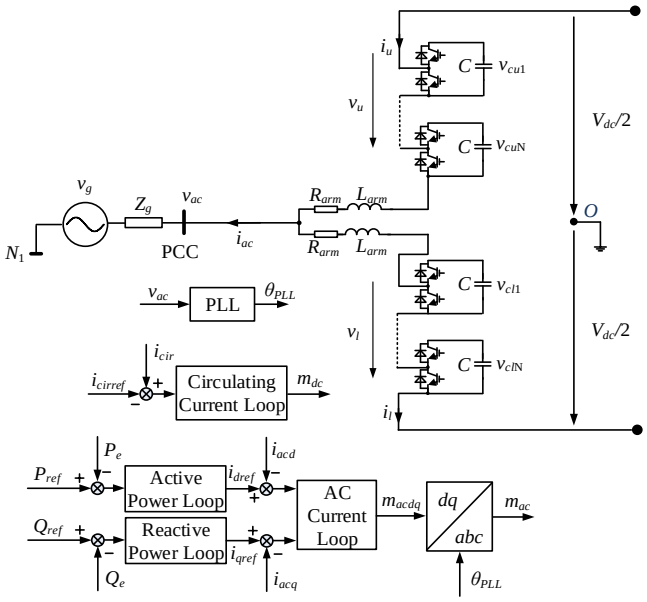

Figure 3.2. Single-phase diagram of the grid-connected MMC with GFL control. Source: [J2].

Fig. 3.2 shows the system diagram of the grid-connected MMC with GFL control. The dynamics of control loops can be generally expressed as

$$\hat{\mathbf{m}}_{\alpha\beta+-0} = \mathbf{G}_x \hat{\mathbf{x}}_{\alpha\beta+-0} + \mathbf{G}_v \hat{\mathbf{v}}_{\alpha\beta+-0} . \tag{3.12}$$

where

$$\begin{aligned} \hat{\mathbf{m}}_{\alpha\beta+-0} &= \left[\hat{M}_{-h} \quad \ldots \quad \hat{M}_{-1} \quad \hat{M}_0 \quad \hat{M}_1 \quad \ldots \quad \hat{M}_h \right]^T \\ \hat{M}_h &= \left[\hat{m}_{ac\alpha\beta+-0}(s + jh\omega_0) \quad \hat{m}_{dc\alpha\beta+-0}(s + jh\omega_0) \right]^T \end{aligned} . \tag{3.13}$$

$$\begin{aligned} \hat{\mathbf{v}}_{\alpha\beta+-0} &= \left[\hat{V}_{-h} \quad \ldots \quad \hat{V}_{-1} \quad \hat{V}_0 \quad \hat{V}_1 \quad \ldots \quad \hat{V}_h \right]^T \\ \hat{V}_h &= \left[\hat{v}_{ac\alpha\beta+-0}(s + jh\omega_0) \quad \hat{v}_{dc\alpha\beta+-0}(s + jh\omega_0) \right]^T \end{aligned} . \tag{3.14}$$

$\mathbf{G_x}$ and $\mathbf{G_v}$ are determined by control loops, and will be derived in the following.

Substituting (3.12) into (3.7), the small-signal model of the MMC can be generally expressed as:

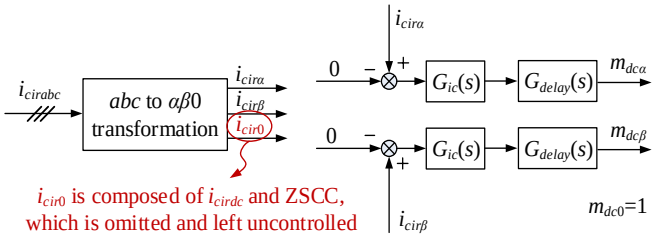

Figure 3.3. Block diagram of the classical CCSC without the ZSCC control. Source: [J2]

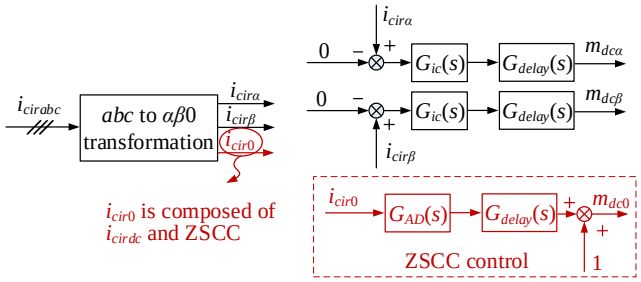

Figure 3.4. Block diagram of the CCSC with the ZSCC control. Source: [J2]

$$\begin{aligned} s\hat{\mathbf{x}}_{\alpha\beta+-0} &= \left(\mathbf{A}_{\mathbf{hss}\alpha\beta+-0} + \mathbf{B}_{\mathbf{mhss}\alpha\beta+-0}\mathbf{G}_{\mathbf{x}}\right)\hat{\mathbf{x}}_{\alpha\beta+-0} \\ &+\left(\mathbf{B}_{\mathbf{mhss}\alpha\beta+-0}\mathbf{G}_{\mathbf{v}} + \mathbf{B}_{\mathbf{vhss}\alpha\beta+-0}\right)\hat{\mathbf{v}}_{\alpha\beta+-0} \end{aligned} . \tag{3.15}$$

where $\mathbf{B}_{\mathbf{mhss}\alpha\beta+-0}$ and $\mathbf{B}_{\mathbf{vhss}\alpha\beta+-0}$ are submatrices of $\mathbf{B}_{\mathbf{hss}\alpha\beta+-0}$ in (3.11).

Fig. 3.3 shows the commonly used CCSC without the ZSCC control [59], where $G_{delay}(s)$ represents the time delay in the CCSC and $G_{ic}(s)$ is the circulating current regulator. The dynamics of the classical CCSC can be expressed as

$$\begin{aligned} \begin{bmatrix} \hat{m}_{dc\alpha}(s) \\ \hat{m}_{dc\beta}(s) \\ \hat{m}_{dc0}(s) \end{bmatrix} &= \begin{bmatrix} G_{ic}(s)G_{delay}(s) & & \\ & G_{ic}(s)G_{delay}(s) & \\ & & 0 \end{bmatrix} \begin{bmatrix} \hat{i}_{cir\alpha}(s) \\ \hat{i}_{cir\beta}(s) \\ \hat{i}_{cir0}(s) \end{bmatrix} \\ &\triangleq \mathbf{G}_{\mathbf{tfcir}} \begin{bmatrix} \hat{i}_{cir\alpha}(s) \\ \hat{i}_{cir\beta}(s) \\ \hat{i}_{cir0}(s) \end{bmatrix} \end{aligned} . \tag{3.16}$$

and its complex-valued representation is given by

$$\begin{bmatrix} \hat{m}_{dc\alpha\beta+}(s) \\ \hat{m}_{dc\alpha\beta-}(s) \\ \hat{m}_{dc\alpha\beta0}(s) \end{bmatrix} = T_1 \mathbf{G}_{\mathbf{tfcir}} T_1^{-1} \begin{bmatrix} \hat{i}_{cir\alpha\beta+}(s) \\ \hat{i}_{cir\alpha\beta-}(s) \\ \hat{i}_{cir0}(s) \end{bmatrix}. \tag{3.17}$$

Fig .3.4 shows the CCSC with the ZSCC control [34]-[35], where $G_{AD}(s)$ is the active damping controller, which is expressed as:

$$G_{AD}(s) = R_{AD} \frac{s}{s+\omega_{AD}}. \tag{3.18}$$

Based on Fig .3.4, the dynamics of the CCSC with the ZSCC control can be expressed as

$$\begin{aligned} \begin{bmatrix} \hat{m}_{dc\alpha}(s) \\ \hat{m}_{dc\beta}(s) \\ \hat{m}_{dc0}(s) \end{bmatrix} &= \begin{bmatrix} G_{ic}(s)G_{delay}(s) & & \\ & G_{ic}(s)G_{delay}(s) & \\ & & G_{AD}(s)G_{delay}(s) \end{bmatrix} \begin{bmatrix} \hat{i}_{cir\alpha}(s) \\ \hat{i}_{cir\beta}(s) \\ \hat{i}_{cir0}(s) \end{bmatrix} \\ &\triangleq \mathbf{G}_{\mathbf{tfcirz}} \begin{bmatrix} \hat{i}_{cir\alpha}(s) \\ \hat{i}_{cir\beta}(s) \\ \hat{i}_{cir0}(s) \end{bmatrix} \end{aligned}. \tag{3.19}$$

The complex-vector representation of (3.19) is given by

$$\begin{bmatrix} \hat{m}_{dc\alpha\beta+}(s) \\ \hat{m}_{dc\alpha\beta-}(s) \\ \hat{m}_{dc\alpha\beta0}(s) \end{bmatrix} = T_1 \mathbf{G}_{\mathbf{tfcirz}} T_1^{-1} \begin{bmatrix} \hat{i}_{cir\alpha\beta+}(s) \\ \hat{i}_{cir\alpha\beta-}(s) \\ \hat{i}_{cir0}(s) \end{bmatrix}. \tag{3.20}$$

Figs. 3.5 and 3.6 show the block diagram of the active/reactive power loops and the ac current loop, respectively, and their dynamics are expressed as:

$$\begin{aligned} \begin{bmatrix} \hat{i}_{dref} \\ \hat{i}_{qref} \end{bmatrix} &= -\begin{bmatrix} G_p(s)G_{LPFp}(s) & \\ & G_q(s)G_{LPFq}(s) \end{bmatrix} \begin{bmatrix} \hat{p}_e \\ \hat{q}_e \end{bmatrix} \\ &\triangleq -\begin{bmatrix} G_{p1}(s) & \\ & G_{q1}(s) \end{bmatrix} \begin{bmatrix} \hat{p}_e \\ \hat{q}_e \end{bmatrix} \end{aligned}. \tag{3.21}$$

$$\begin{bmatrix} \hat{m}_{acd}^{c} \\ \hat{m}_{acq}^{c} \end{bmatrix} = \begin{bmatrix} G_{id}(s)G_{delay}(s) & \\ & G_{id}(s)G_{delay}(s) \end{bmatrix} \begin{bmatrix} \hat{i}_{refd} - \hat{i}_{acd}^{c} \\ \hat{i}_{refq} - \hat{i}_{acq}^{c} \end{bmatrix} \triangleq \begin{bmatrix} G_{id1}(s) & \\ & G_{id1}(s) \end{bmatrix} \begin{bmatrix} \hat{i}_{refd} - \hat{i}_{acd}^{c} \\ \hat{i}_{refq} - \hat{i}_{acq}^{c} \end{bmatrix}. \tag{3.22}$$

It is known from Fig. 3.5 and 3.6 that the active/reactive power control loops and the ac current loop are implemented in the dq frame whose orientation is determined by the phase-locked loop (PLL), which is defined as the *controller-dq frame* [16]. In order to capture the synchronization dynamics of the PLL, the model should be finally transformed to the *system-dq* frame whose orientation is determined by the grid phase angle [16]. The transformation of state variables from the *controller-dq frame* ($\hat{x}_{dq+}^{c}$ and $\hat{x}_{dq-}^{c}$) to the *system-dq frame* ($\hat{x}_{dq+}^{s}$ and $\hat{x}_{dq-}^{s}$) is given by [16].

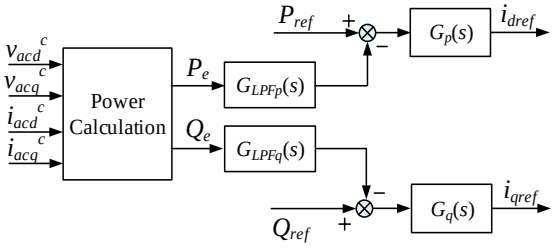

Figure 3.5. Block diagram of the active and reactive power loop. Source: [J2].

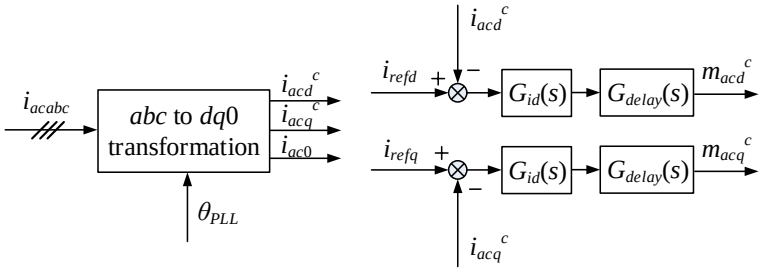

Figure 3.6. Block diagram of the ac current control loop. Source: [J2].

$$\begin{bmatrix} \hat{x}^s_{dq+} \\ \hat{x}^s_{dq-} \end{bmatrix} = \begin{bmatrix} \hat{x}^c_{dq+} \\ \hat{x}^c_{dq-} \end{bmatrix} + \frac{G_{PLL}}{2} \begin{bmatrix} X^s_d + jX^s_q & -\left(X^s_d + jX^s_q\right) \\ -\left(X^s_d - jX^s_q\right) & X^s_d - jX^s_q \end{bmatrix} \begin{bmatrix} \hat{v}^s_{acdq+} \\ \hat{v}^s_{acdq-} \end{bmatrix}. \tag{3.23}$$

where G_{PLL} is the transfer function of the PLL [J2]. The superscript *s* represents the variables in the *system-dq* frame, while the superscript *c* denotes the variables in the *controller-dq* frame [J2].

In [J2], a step-by-step modeling procedure of control loops of the GFL-MMC is given, which is summarized in Fig. 3.7, following which, control loops represented by real vectors in the *controller-dq frame*, i.e., (3.21) and (3.22), can be equivalently transformed to the complex-vector representation in the *system-αβ frame*, which is given by

$$\begin{bmatrix} \hat{m}^s_{ac\alpha\beta+}(s) \\ \hat{m}^s_{ac\alpha\beta-}(s-2j\omega_0) \end{bmatrix} = \mathbf{H_x}(\mathbf{s-j\omega_0}) \begin{bmatrix} \hat{i}^s_{ac\alpha\beta+}(s) \\ \hat{i}^s_{ac\alpha\beta-}(s-2j\omega_0) \end{bmatrix} + \mathbf{H_v}(\mathbf{s-j\omega_0}) \begin{bmatrix} \hat{v}^s_{ac\alpha\beta+}(s) \\ \hat{v}^s_{ac\alpha\beta-}(s-2j\omega_0) \end{bmatrix}. \tag{3.24}$$

where $\mathbf{H_x}$ and $\mathbf{H_v}$ are given by (C.1) and (C.2) in [J2].

1. Model the control loop of the MMC based on the **real vector** in the **controller dq frame** $\left(\hat{x}^c_d,\ \hat{x}^c_q,\ \hat{x}_0\right)$

$$\Downarrow \quad \begin{bmatrix} \hat{x}^c_{dq+} \\ \hat{x}^c_{dq-} \\ \hat{x}_0 \end{bmatrix} = \begin{pmatrix} 1 & j & \\ 1 & -j & \\ & & 1 \end{pmatrix} \begin{bmatrix} \hat{x}^c_d \\ \hat{x}^c_q \\ \hat{x}_0 \end{bmatrix}$$

2. Transfer the model to the **complex vector** representation in the **controller dq frame** $\left(\hat{x}^c_{dq+},\ \hat{x}^c_{dq-},\ \hat{x}_0\right)$

$$\Downarrow \quad \begin{bmatrix} \hat{x}^s_{dq+} \\ \hat{x}^s_{dq-} \end{bmatrix} = \begin{bmatrix} \hat{x}^c_{dq+} \\ \hat{x}^c_{dq-} \end{bmatrix} + \frac{G_{PLL}}{2} \begin{bmatrix} X^s_d + jX^s_q & -\left(X^s_d + jX^s_q\right) \\ -\left(X^s_d - jX^s_q\right) & X^s_d - jX^s_q \end{bmatrix} \begin{bmatrix} \hat{v}^s_{acdq+} \\ \hat{v}^s_{acdq-} \end{bmatrix}$$

3. Transfer the model to the **complex vector** representation in the **system dq frame** $\left(\hat{x}^s_{dq+},\ \hat{x}^s_{dq-},\ \hat{x}_0\right)$

$$\Downarrow \quad \begin{bmatrix} \hat{x}^s_{\alpha\beta+} \\ \hat{x}^s_{\alpha\beta-} \\ \hat{x}_0 \end{bmatrix} = \begin{pmatrix} e^{j\omega_0 t} & & \\ & e^{-j\omega_0 t} & \\ & & 1 \end{pmatrix} \begin{bmatrix} \hat{x}^s_{dq+} \\ \hat{x}^s_{dq-} \\ \hat{x}_0 \end{bmatrix}$$

4. Transfer the model to the **complex vector** representation in the **system *αβ* frame** $\left(\hat{x}^s_{\alpha\beta+},\ \hat{x}^s_{\alpha\beta-},\ \hat{x}_0\right)$

Figure 3.7. Step-by-step modeling procedure of control loops of the GFL-MMC. Source: [J2]

The closed-loop model of the GFL-MMC with/without the ZSCC control can be obtained by substituting (3.17), (3.20) and (3.24) into (3.15).

3.3. Stability Impact of the ZSCC Control

The admittance (impedance) matrix of the MMC, which characterizes the relationship between $\hat{v}_{ac\alpha\beta+-}(s+jh\omega_0)$ and $\hat{i}_{ac\alpha\beta+-}(s+jh\omega_0)$, can be derived from (3.15), which is given by

$$\hat{\mathbf{i}}_{\mathbf{ac}} = \mathbf{Y}_{\mathbf{MMC}}\hat{\mathbf{v}}_{\mathbf{ac}}$$

$$\mathbf{Y}_{\mathbf{MMC}} = \begin{bmatrix} \ddots & & \vdots & \vdots & & \iddots \\ & Y_{0pp}(s-j\omega_0) & Y_{0cpn}(s-j\omega_0) & Y_{-1pp}(s) & Y_{-1cpn}(s) & Y_{-2pp}(s+j\omega_0) & Y_{-2cpn}(s+j\omega_0) & \\ & Y_{0cnp}(s-j\omega_0) & Y_{0nn}(s-j\omega_0) & Y_{-1cnp}(s) & Y_{-1nn}(s) & Y_{-2cnp}(s+j\omega_0) & Y_{-2nn}(s+j\omega_0) & \\ \cdots & Y_{1pp}(s-j\omega_0) & Y_{1cpn}(s-j\omega_0) & Y_{0pp}(s) & Y_{0cpn}(s) & Y_{-1pp}(s+j\omega_0) & Y_{-1cpn}(s+j\omega_0) & \cdots \\ \cdots & Y_{1cnp}(s-j\omega_0) & Y_{1nn}(s-j\omega_0) & Y_{0cnp}(s) & Y_{0nn}(s) & Y_{-1cnp}(s+j\omega_0) & Y_{-1nn}(s+j\omega_0) & \cdots \\ & Y_{2pp}(s-j\omega_0) & Y_{2cpn}(s-j\omega_0) & Y_{1pp}(s) & Y_{1cpn}(s) & Y_{0pp}(s+j\omega_0) & Y_{0cpn}(s+j\omega_0) & \\ & Y_{2cnp}(s-j\omega_0) & Y_{2nn}(s-j\omega_0) & Y_{1cnp}(s) & Y_{1nn}(s) & Y_{0cnp}(s+j\omega_0) & Y_{0nn}(s+j\omega_0) & \\ \iddots & & \vdots & \vdots & & \ddots \end{bmatrix} \tag{3.25}$$

$$\hat{\mathbf{i}}_{\mathbf{ac}} = \begin{bmatrix} \cdots & \hat{i}_{ac\alpha\beta+}(s-j\omega_0) & \hat{i}_{ac\alpha\beta-}(s-j\omega_0) & \hat{i}_{ac\alpha\beta+}(s) & \hat{i}_{ac\alpha\beta-}(s) & \hat{i}_{ac\alpha\beta+}(s+j\omega_0) & \hat{i}_{ac\alpha\beta-}(s+j\omega_0) & \cdots \end{bmatrix}^T$$

$$\hat{\mathbf{v}}_{\mathbf{ac}} = \begin{bmatrix} \cdots & \hat{v}_{ac\alpha\beta+}(s-j\omega_0) & \hat{v}_{ac\alpha\beta-}(s-j\omega_0) & \hat{v}_{ac\alpha\beta+}(s) & \hat{v}_{ac\alpha\beta-}(s) & \hat{v}_{ac\alpha\beta+}(s+j\omega_0) & \hat{v}_{ac\alpha\beta-}(s+j\omega_0) & \cdots \end{bmatrix}^T$$

.

$$\mathbf{Z}_{\mathbf{MMC}} = \mathbf{Y}_{\mathbf{MMC}}^{-1} = \begin{bmatrix} \ddots & & \vdots & \vdots & & \iddots \\ & Z_{0pp}(s-j\omega_0) & Z_{0cpn}(s-j\omega_0) & Z_{-1pp}(s) & Z_{-1cpn}(s) & Z_{-2pp}(s+j\omega_0) & Z_{-2cpn}(s+j\omega_0) & \\ & Z_{0cnp}(s-j\omega_0) & Z_{0nn}(s-j\omega_0) & Z_{-1cnp}(s) & Z_{-1nn}(s) & Z_{-2cnp}(s+j\omega_0) & Z_{-2nn}(s+j\omega_0) & \\ \cdots & Z_{1pp}(s-j\omega_0) & Z_{1cpn}(s-j\omega_0) & Z_{0pp}(s) & Z_{0cpn}(s) & Z_{-1pp}(s+j\omega_0) & Z_{-1cpn}(s+j\omega_0) & \cdots \\ \cdots & Z_{1cnp}(s-j\omega_0) & Z_{1nn}(s-j\omega_0) & Z_{0cnp}(s) & Z_{0nn}(s) & Z_{-1cnp}(s+j\omega_0) & Z_{-1nn}(s+j\omega_0) & \cdots \\ & Z_{2pp}(s-j\omega_0) & Z_{2cpn}(s-j\omega_0) & Z_{1pp}(s) & Z_{1cpn}(s) & Z_{0pp}(s+j\omega_0) & Z_{0cpn}(s+j\omega_0) & \\ & Z_{2cnp}(s-j\omega_0) & Z_{2nn}(s-j\omega_0) & Z_{1cnp}(s) & Z_{1nn}(s) & Z_{0cnp}(s+j\omega_0) & Z_{0nn}(s+j\omega_0) & \\ \iddots & & \vdots & \vdots & & \ddots \end{bmatrix}. \tag{3.26}$$

The frequency coupling terms in (3.25) and (3.26) should be considered during the stability analysis, instead of using the Generalized Nyquist Stability Criterion (GNSC), a more intuitive criterion is used in [J2] by analyzing the closed-loop SISO equivalent impedance ratio, which is detailed as follows.

Considering the three-phase balanced grid whose impedance matrix is diagonal, i.e.,

$$\mathbf{Z}_{\mathbf{g}} = \mathrm{diag}\left[Z_{g\alpha\beta+}(s-2j\omega_0) \quad \cdots \quad Z_{g\alpha\beta+}(s) \quad \cdots \quad Z_{g\alpha\beta-}(s+2j\omega_0) \right]. \tag{3.27}$$

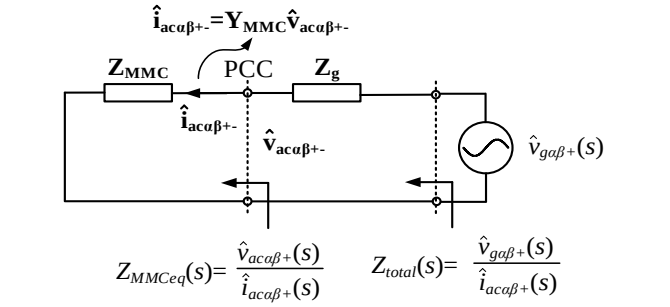

(a)

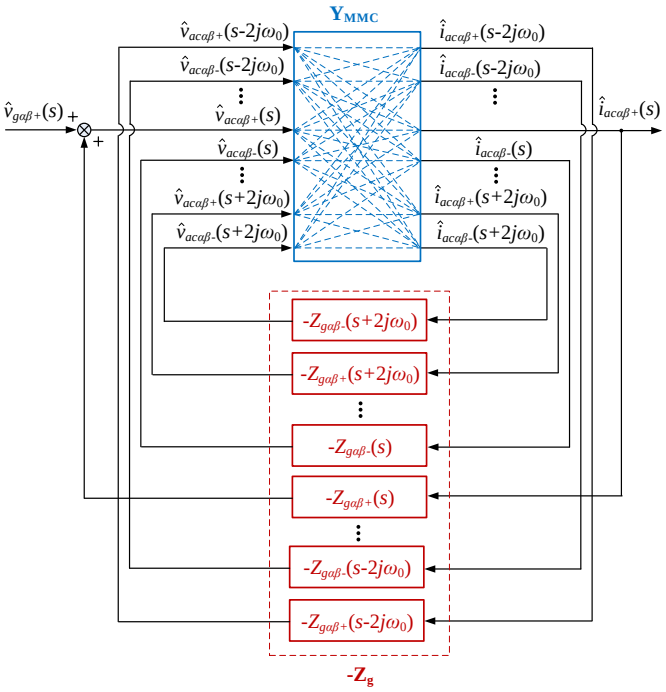

(b)

Figure 3.8. Closed-loop representation of the MMC-grid system. (a) Small-signal equivalent circuit. (b) Block diagram with cross couplings. Source: [J2].

Fig. 3.8 (a) shows the closed-loop equivalent circuit of the MMC-grid system, whereas its block diagram is given in Fig. 3.8 (b), based on which, the closed-loop SISO equivalent impedance of the MMC can be derived, which is given by:

$$Z_{MMCeq}(s) = 1/Y_{total}(s) - Z_{g\alpha\beta+}(s). \tag{3.28}$$

where

$$Y_{total}(s) = \frac{\hat{i}_{ac\alpha\beta+}(s)}{\hat{v}_{g\alpha\beta+}(s)} = \mathbf{Y_{close}}(5,5). \tag{3.29}$$

$$\mathbf{Y_{close}} = \left(\mathbf{I} + \mathbf{Y_{MMC}}\mathbf{Z_g}\right)^{-1}\mathbf{Y_{MMC}}. \tag{3.30}$$

Based on (3.28), the closed-loop SISO representation of Fig. 3.8 (b) is derived, as illustrated in Fig. 3.9. It is clear that the system stability can be assessed by checking the loop gain $Z_{g\alpha\beta+}(s)/Z_{MMCeq}(s)$. Moreover, $Z_{MMCeq}(s)$ is derived considering the frequency-coupled impedances and the grid impedance, which is different from the centered-diagonal element $[Z_{0pp}(s)]$ in (3.26).

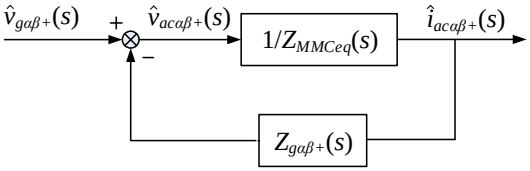

Figure 3.9. SISO equivalent block diagram of the MMC system. Source: [J2].

Table 3.1. Main Circuit Parameters of the MMC. Source: [J2]

SYMBOL	DESCRIPTION	VALUE
V_{grms}	RMS value of grid voltage (line to line)	100 kV
f_g	Grid frequency	50 Hz
P_o	Rated output power	100 MW
V_{dc}	DC side voltage	±100 kV
L_{arm}	Arm inductance	45 mH
R_{arm}	Arm resistance	0.15 Ω
C_{sm}	Capacitance of the submodule	3.3 mF
N	Number of the submodule each arm	100

Table 3.2. Controller Parameters of the MMC. Source: [J2]

	SYMBOL	VALUE
Active Power Loop	K_{pp}	$8.2\cdot10^{-6}$ /V
	K_{pi}	$1.3\cdot10^{-4}$ /(V·s)
	ω_p	10π rad/s
Reactive Power Loop	K_{qp}	$8.2\cdot10^{-6}$ /V
	K_{qi}	$2.6\cdot10^{-4}$ /(V·s)
	ω_q	10π rad/s
PLL	K_{pPLL}	$2.6\cdot10^{-3}$ rad/(s·V)
	K_{iPLL}	0.29 rad/(s^2·V)
AC Current Loop	K_{Pid}	$6.3\cdot10^{-4}\,\Omega$
	K_{iid}	0.32 Ω/s
Circulating Current Loop	K_{pic}	$9.4\cdot10^{-4}\,\Omega$
	K_{Ric}	$2.8\cdot10^{-3}\,\Omega$/s
	ω_{AD}	10π rad/s
Control Delay	T_d	200 μs

Fig. 3.10 shows the comparison between $Z_{0pp}(s)$ and $Z_{MMCeq}(s)$. The main circuit and controller parameters of the MMC are given in Table 3.1 and 3.2, respectively. The significant difference in the magnitude and phase angle of $Z_{0pp}(s)$ and $Z_{MMCeq}(s)$ in the low-frequency range can be clearly observed in the zoom-in figures, which indicates that using $Z_{0pp}(s)$ only in the stability analysis will lead to the inaccurate stability predictions.

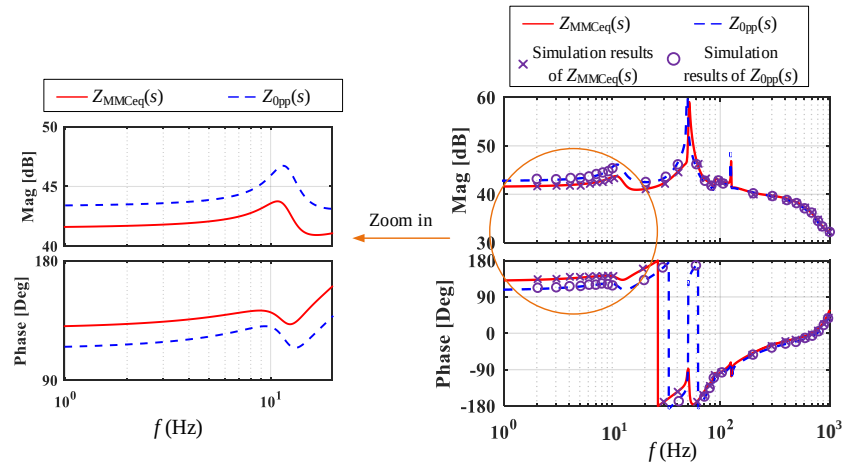

(a)

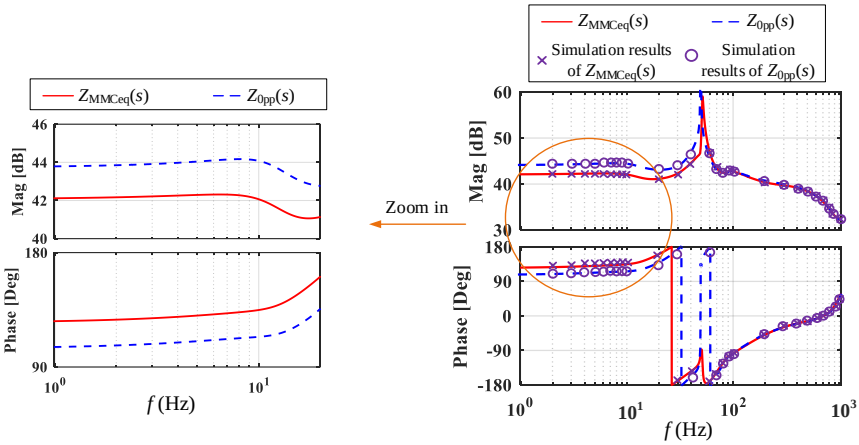

(b)

Figure 3.10. Bode diagrams of $Z_{0pp}(s)$ and $Z_{MMCeq}(s)$. (a) Without the ZSCC control. (b) With the ZSCC control (R_{AD}=2×10^{-2} pu). Source: [J2].

Fig. 3.11 shows the Bode diagram of $Z_{MMCeq}(s)$ and $Z_g(s)$ (0.5 pu inductance) with/without the ZSCC control, it can be seen from Fig. 3.11 (a) that the additional resonant peak in $Z_{MMCeq}(s)$ is yielded due to the absence of the ZSCC control, which leads to the phase difference at the magnitude intersection point to be 189° > 180°, and thus, the system is unstable. In contrast, this resonant peak can be effectively damped by using the ZSCC control and the system is stabilized, as shown in Fig. 3.11

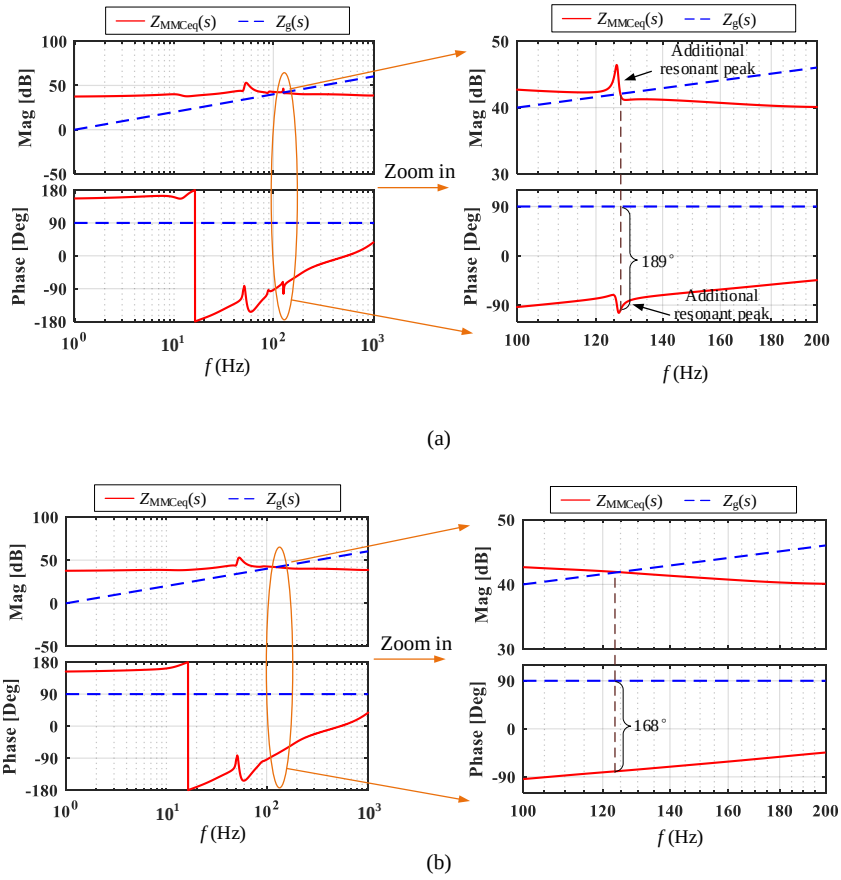

Figure 3.11. Bode diagram of $Z_{MMCeq}(s)$ and $Z_g(s)$. (a) Without the ZSCC control. (b) With the ZSCC control (R_{AD}=2×10^{-2} pu). Source: [J2]

(b). The detailed parameters tuning guideline for stabilizing the MMC system under the weak grid condition can be found in [J2].

3.4. Case Studies

In order to verify the theoretical analysis, time-domain simulations are carried out by adopting the parameters given in Table 3.1 and 3.2. Fig. 3.12 shows the simulation results of the MMC with/without the ZSCC control under the stiff grid where $Z_g(s)$=0. It can be seen that the MMC can be operated stably in both cases, where the 2nd-order harmonic in the circulating current can also be effectively suppressed.

Fig. 3.13 shows the simulation results of the MMC with/without the ZSCC control under the weak grid where $Z_g(s)$=0.5 pu. It can be seen that the MMC might become unstable if the ZSCC control is not used, as shown in Fig. 3.13 (a), where the zero sequence oscillation in the circulating current can be clearly observed. In contrast, the system can be stabilized by using the ZSCC control, as shown in Fig. 3.13 (b). The simulation results given in Fig. 3.13 corroborate the theoretical study in Fig. 3.11.

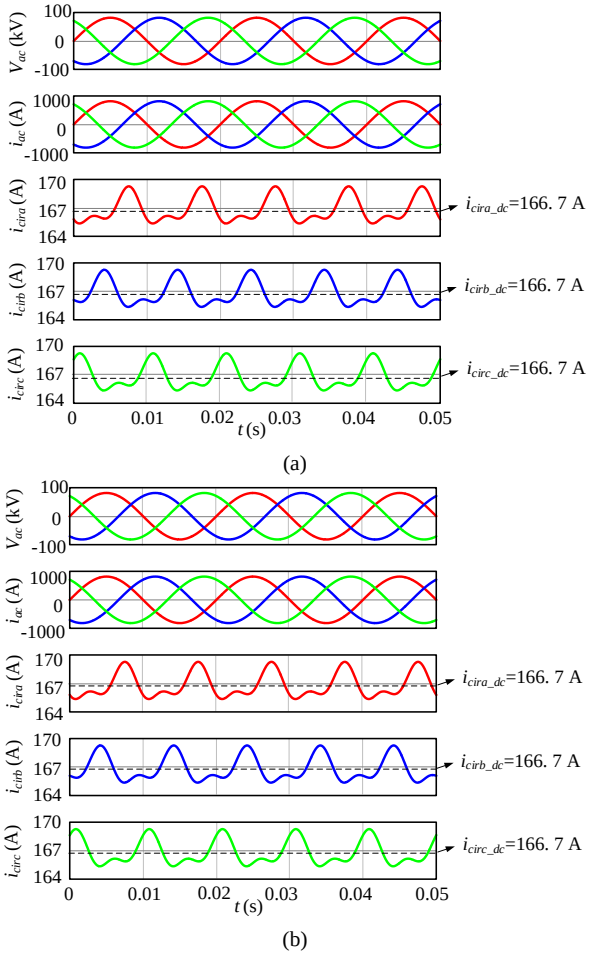

Figure 3.12. Time-domain simulation results of the MMC connecting to the strong ac grid [$Z_g(s)$=0]. (a) Without the ZSCC control, stable. (b) With the ZSCC control and $R_{AD}=2\times10^{-2}$ pu, stable. Source: [J2]

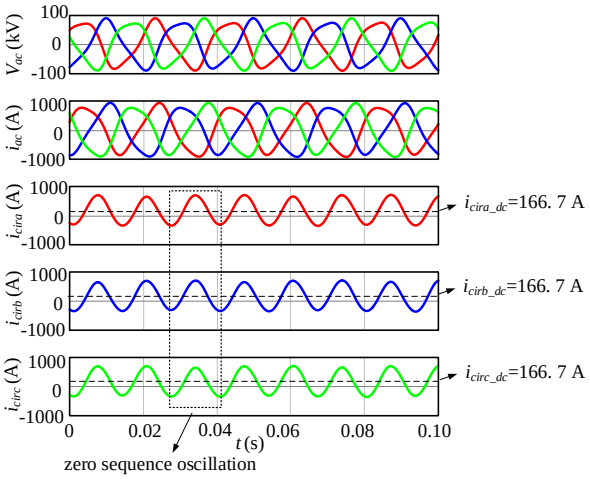

(a)

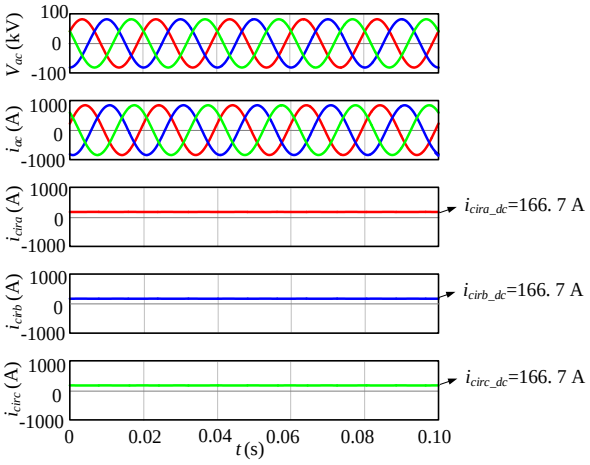

(b)

Figure 3.13. Time-domain simulation results of the MMC connecting to the weak ac grid [$Z_g(s)$=0.5 pu]. (a) Without the ZSCC control, unstable. (b) With the ZSCC control and R_{AD}=2×10^{-2} pu, stable. Source: [J2].

3.5. Summary

This chapter develops the complex-vector based small-signal model of the GFL-MMC, based on which, the closed-loop SISO ac equivalent impedance of the MMC with/without the ZSCC control is thoroughly compared. It is revealed that the additional resonant peak is yielded in this equivalent impedance of the MMC due to

the absence of the ZSCC control, which may destabilize the MMC under the weak ac grid. This conclusion reveals the necessity of using the ZSCC control for the stable operation of the MMC. All the theoretical findings are corroborated by time-domain simulations.

Chapter 4. Transient Stability of GFM-VSCs with Power Synchronization Control

The content of this chapter is based on **J3 and C2**.

4.1. Background

The ever increasing integration of voltage-source converters (VSCs) into the power system poses new challenges to its stability [3]. Although GFL-VSCs are still dominated in the field application, it can hardly be stabilized under the very weak grid whose short circuit ratio (SCR) approaches 1.3, owing to the negative damping introduced by the phase-locked loop (PLL) [60]. To deal with this issue, the concept of the GFM-VSC, which utilizes the active power loop (APL), rather than the PLL for the grid synchronization, has been proposed [10].

The power synchronization control (PSC) is one of the typical control architectures of GFM-VSCs [40]. The PSC-VSC can be operated stably under the ultra-weak grid where the SCR approaches 1 [43], and thus, it has been wildly used [41]-[42].

In [40]-[44], the small-signal stability of the PSC-VSC has been thoroughly investigated, and its superior small-signal dynamics over the GFL-VSC has been clearly identified. In contrast, less attention has been attracted on the transient stability (synchronization stability under large disturbances) of the PSC-VSC. Although the transient stability analysis of the synchronous generator (SG) is a mature topic, the research results cannot be directly borrowed due to the different dynamics between the PSC-VSC and the SG. The APL of the PSC-VSC is the first-order control loop [40], while the power angle swing equation of the SG exhibits the second-order dynamics [1].

To fill this void, a systematic transient stability analysis of the PSC-VSC is performed in our work [J3]. In order to avoid the difficulty of solving the nonlinear differential equations, the phase portrait is utilized to provide a graphical solution for the trajectory of the PSC-VSC after disturbances. It is revealed that the PSC-VSC has a superior transient performance over the SG, thanks to its first-order power angle control. All the findings are finally corroborated by experimental tests. The main content of [J3] is summarized as follows.

4.2. Transient Stability Basics of the SG

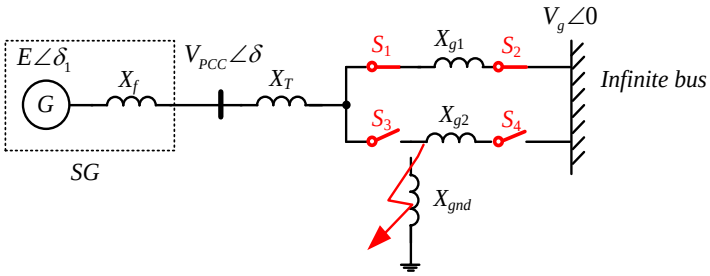

Figure 4.1. The SG connecting to the infinite bus. Source: [J3].

In order to facilitate the transient stability study of the PSC-VSC, two typical transient stability problems are identified in this part by reviewing the basic transient stability characteristic of the SG.

Fig. 4.1 shows the circuit diagram of the SG connecting to the power grid, the swing equation and the output power of the SG can be expressed as [1]

$$P_m - P_e - D\dot{\delta} = J\omega_n\ddot{\delta}\,. \tag{4.1}$$

$$P_e = \frac{3V_{PCC}V_g}{2X_g}\sin\delta\,. \tag{4.2}$$

where P_m, P_e, J and D are the input mechanical power, output electrical power, inertia, and damping coefficient of the SG, respectively. V_{PCC} and V_g are magnitudes of the voltage at the point of common coupling (PCC) and the grid voltage, respectively. X_g represents the equivalent grid impedance. δ is the power angle, which is defined as the angle difference between the PCC voltage and the grid voltage.

Based on (4.2), the P_e-δ curves before disturbances can be plotted as dashed lines in Fig. 4.2 (a) and (b). The SG initially operates at the stable equilibrium point (SEP) *a* where $P_m = P_e$.

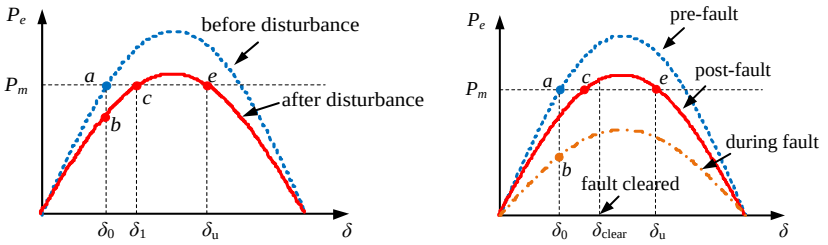

Figure 4.2. P_e-δ curves. (a) Type-I transient stability problem: with equilibrium points after the transient disturbance, dashed line: before disturbance, solid line: after disturbance. (b) Type-II transient stability problem: without equilibrium points during the transient disturbance, dashed line: pre-fault, dashed dotted line: during fault, solid line: post-fault. Source: [J3].

Based on the existence of equilibrium points after disturbances, the transient stability problems are categorized as Type-I (with equilibrium points) and Type-II (without equilibrium points), and the corresponding P_e-δ curves after disturbances are illustrated as the solid line in Fig. 4.2 (a) and the dashed dotted line in Fig. 4.2 (b), respectively. For the Type-II transient stability problem, the system can only be stabilized after the equilibrium points are restored by the fault clearance [1], as the solid line shown in Fig. 4.2 (b). The largest fault clearing angle and time (FCA and FCT) which prevent the transient instability of the system are known as the critical clearing angle (CCA) and the critical clearing time (CCT) [1].

It is known from (4.1) that the rotor of the SG will accelerate whenever $P_m > P_e$, and decelerate whenever $P_m < P_e$. Therefore, the sufficient and necessary condition for the transient stability of the SG is no crossing of the unstable equilibrium point (UEP) *e* in Fig 4.2, otherwise the SG will keep accelerating after the UEP *e* because of $P_m > P_e$, and the loss of synchronization (LOS) is inevitable.

4.3. Transient Stability Analysis of the PSC-VSC

Fig. 4.3 shows the circuit and control diagram of the PSC-VSC, the PCC voltage v_{PCC} is regulated by the inner voltage control loop to accurately track its reference value v_{PCCref}. V_{mref} denotes the magnitude of v_{PCCref}, which is fixed as 1.0 p.u. when the PSC-VSC is operated in the alternating-voltage control (AVC) mode [40]. θ_{ref} represents the phase angle of v_{PCCref} and is generated by the PSC, which is given by:

$$\theta_{ref} = K_i \int \left(P_{ref} - P_e \right) + \omega_0 t \,. \tag{4.3}$$

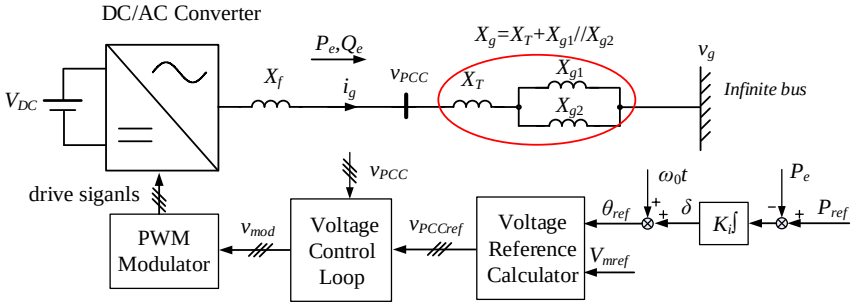

Figure 4.3. Circuit and Control diagram of the PSC-VSC under the normal operation, where its output current is within the current limit. Source: [J3].

where P_{ref} and P_e are the active power reference and the output active power for the PSC-VSC, respectively. The expression of P_e is given by (4.2). ω_0 represents the grid frequency and K_i is the integral gain of the PSC.

It is worth noting that the dynamics of the inner voltage control loop is usually designed 10 times faster than that of outer power control loops which dominate the transient stability of the PSC-VSC [18],[52], and thus, v_{PCC}=v_{PCCref} can be assumed during the transient stability analysis [39]. Moreover, only the transient disturbances that do not provoke current limit control of the PSC-VSC is considered in this chapter. The transient stability of the PSC-VSC when it is switched to the current limit control will be detailed in next chapter.

Considering the grid phase $\theta_g=\omega_0 t$, the power angle δ can be calculated as

$$\delta = \theta_{ref} - \theta_g = K_i \int \left(P_{ref} - P_e \right) + \omega_0 t - \omega_0 t = K_i \int \left(P_{ref} - P_e \right). \tag{4.4}$$

Substituting (4.2) into (4.4) and considering the assumption of V_{PCC}=V_{mref}, which yields

$$\dot{\delta} = K_i \left(P_{ref} - \frac{3V_{PCC}V_g}{2X_g}\sin\delta \right) = K_i \left(P_{ref} - \frac{3V_{mref}V_g}{2X_g}\sin\delta \right). \tag{4.5}$$

Different from the second-order swing equation of the SG, the first-order dynamics of the PSC-VSC can be clearly observed in (4.5). The first-order PSC will bring in significantly different transient stability characteristic compared to that of the SG, which will be detailed in the next part.

4.3.1. Type-I Transient Stability

Table 4.1. Parameters for the Transient Disturbance Test. Source: [J3].

Parameters			
P_{ref}	1000 MW (1 p.u.)	L_f	0.035 H (0.075 p.u.)
V_g	220 kV/50 Hz (1 p.u.)	K_i	$9.3\cdot10^{-9}$ (0.01 p.u.)
Test case I		Test case II	
L_T	0.01 H (0.02 p.u.)	L_T	0.37 H (0.8 p.u.)
L_{g1}	0.39 H (0.85 p.u.)	L_{g1}	0.07 H (0.15 p.u.)
L_{g2}	0.39 H (0.85 p.u.)	L_{g2}	0.37 H (0.8 p.u.)
		L_{gnd}	0.23 H (0.5 p.u.)

The sudden disconnection of the transmission line 2 (X_{g2} in Fig. 4.3.) is considered in the Type-I transient stability study, and there are equilibrium points after the disturbance. The parameters given in test case I of Table 4.1 are adopted in the analysis.

After the transient disturbances, the system is stable if the power angle δ is converged to the new stable equilibrium point (SEP), and is unstable if δ is diverged. Yet, the nonlinearity of (4.5) complicates the analytical solution of $\delta(t)$. To tackle this challenge, the phase portrait is adopted to provide a graphical solution in a more intuitive manner [61].

Based on (4.5) and parameters of Table 4.1, the phase portraits ($\dot{\delta}-\delta$ curves) of the PSC-VSC before and after disturbances can be directly plotted, which are given as the dashed and solid lines in Fig. 4.4. The line with arrow in Fig. 4.4 indicates the trajectory of δ after the disturbance, i.e., the operating point of the PSC-VSC moves from the point *a* to the point *b* at the instance of the disturbance occurs, after which δ keeps increasing (due to $\dot{\delta}>0$) until the system reaches the new SEP *c*. Because of $\dot{\delta}=0$ at the SEP *c*, the PSC-VSC will stay at the SEP and will not cross over. Thanks to the first-order power angle control of the PSC-VSC, the dynamic response of δ is overdamped, which is significantly different from the oscillatory response of the SG that is determined by the second-order swing equation. The overdamped response of the PSC-VSC guarantees its convergence to the new SEP provided the equilibrium points exist after the disturbance, and thus, the Type-I transient stability problem is avoided.

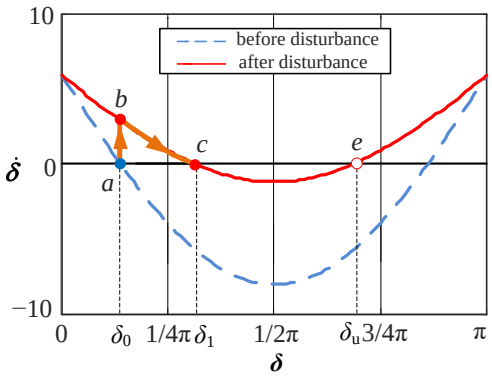

Figure 4.4. Phase portraits of the PSC-VSC before (dashed line) and after (solid line) the transient disturbance for the Type-I transient stability problem. Source: [J3].

4.3.2. Type-II Transient Stability

The three-phase to ground high impedance fault on X_{g2} is considered in the Type-II transient stability study, and the system does not have equilibrium points after the disturbance. The fault is then cleared by disconnecting X_{g2}. The parameters given in the test case II of Table 4.1 are adopted in the analysis.

Fig. 4.5. shows the phase portrait of the PSC-VSC with different FCAs, where the dashed, dash dotted, and solid lines represent the phase portrait pre-, during-, and post-fault, respectively. It is known from Fig. 4.5 (a) that the convergence of the system to the new SEP *c* can be guaranteed as long as FCA $\leq \delta_u$ (the corresponding power angle of the UEP). Therefore, δ_u is defined as the CCA for the PSC-VSC, and it can be calculated as:

$$\mathrm{CCA} = \delta_u = \pi - \arcsin\frac{2P_{ref}X_g}{3V_{mref}V_g}. \tag{4.6}$$

It is clear from (4.6) that the CCA is only related to the post-fault system parameters and is not affected by the fault condition, which makes the design of the protective relay much easier.

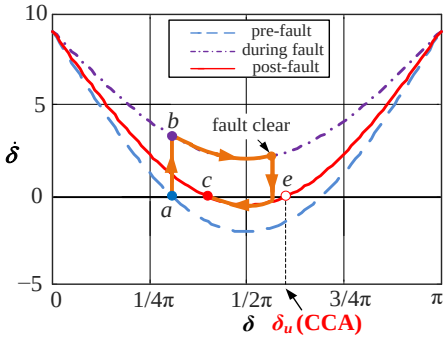

(a)

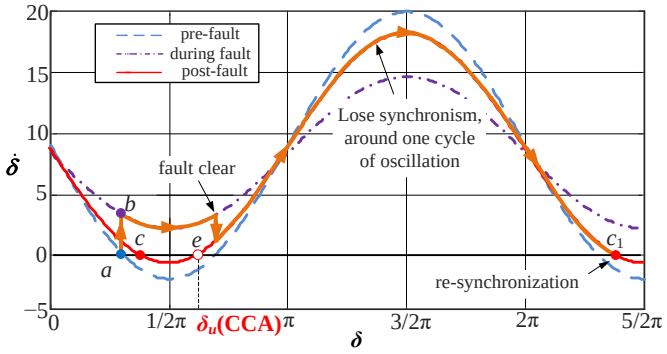

(b)

Figure 4.5. Phase portraits of the PSC-VSC before (dashed line), during (dashed dotted line) and post (solid line) the fault. (a) FCA< δ_u. (b) FCA> δ_u. Source: [J3].

Substituting (4.6) into (4.5), the corresponding CCT can be calculated, which is expressed as:

$$CCT = \frac{2}{\sqrt{a^2-b^2}}\arctan\left[\frac{\tan\left(CCA/2\right)-b/a}{\sqrt{1-\left(b/a\right)^2}}\right] - \frac{2}{\sqrt{a^2-b^2}}\arctan\left[\frac{\tan\left(\delta_0/2\right)-b/a}{\sqrt{1-\left(b/a\right)^2}}\right] \quad (4.7)$$

where δ_0 is the power angle of the new SEP. a and b are expressed as

$$a = K_i P_{ref} \qquad b = K_i \frac{3V_{mref} V_g}{2X_g}. \tag{4.8}$$

Besides the fixed CCA, the PSC-VSC has another promising feature of the re-synchronization capability. Different from the SG, the PSC-VSC will not totally lose the synchronization with the power grid even if the FCA > CCA. Instead, it can still converge to the SEP after around one cycle of oscillation, as indicated by the solid line with arrows in Fig. 4.5 (b). This re-synchronization capability of the PSC-VSC could prevent the system collapse due to the delayed fault clearance.

Table 4.2 compares the transient stability characteristic of the PSC-VSC and the SG, from which the superior transient performance of the PSC-VSC over the SG can be observed.

4.4. Case Studies

The experimental tests are carried out in this part to verify the theoretical analysis. Table 4.3 illustrates the parameters used in the experimental test, whose per unit values are same as that used in the theoretical analysis. The overall experimental setup is illustrated in Fig. 4.6.

Table 4.2. Transient stability of the PSC-VSC and the SG. Source: [J3].

<table>
<tr><th colspan="2">Operating scenarios during the transient disturbance</th><th>Transient stability of the PSC-VSC</th><th>Transient stability of the SG</th></tr>
<tr><td colspan="2">With equilibrium points</td><td>No transient stability problem.</td><td>Risk of the transient instability [1]</td></tr>
<tr><td rowspan="2">No equilibrium points</td><td>Do not trigger the current limitation.</td><td>• Fixed CCA and CCT
• Able to re-synchronize with the power grid even if FCT>CCT</td><td rowspan="2">• CCA and CCT are dependent on fault conditions [1].
• LOS if FCT > CCT [1].</td></tr>
<tr><td>Trigger the current limitation.</td><td>• Switch to the vector current control [40], and the transient stability is mainly determined by the PLL [49]-[51].</td></tr>
</table>

Table 4.3. Parameters for the Experimental Test. Source: [J3].

Parameters			
P_{ref}	1 kW (1 p.u.)	L_f	1.5 mH (0.075 p.u.)
V_g	50 V/50 Hz (1 p.u.)	K_i	$9.3 \cdot 10^{-3}$ (0.01 p.u.)
Test case I		Test case II	
L_T	0.5 mH (0.02 p.u.)	L_T	19 mH (0.8 p.u.)
L_{g1}	21 mH (0.85 p.u.)	L_{g1}	3 mH (0.15 p.u.)
L_{g2}	21 mH (0.85 p.u.)	L_{g2}	19 mH (0.8 p.u.)
		L_{gnd}	12 mH (0.5 p.u.)

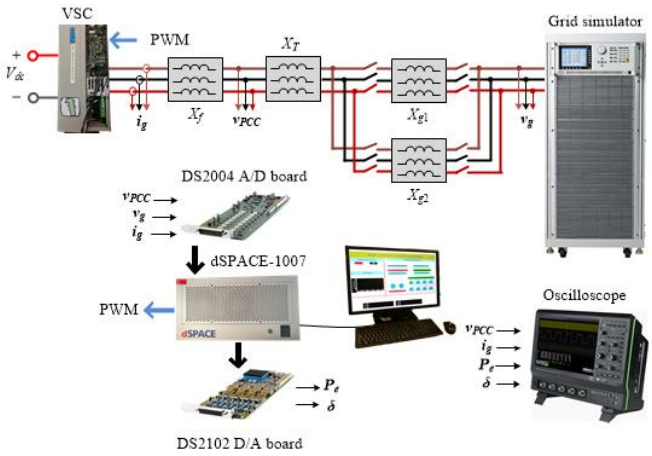

Figure 4.6. Configuration of the experimental setup. Source: [J3].

Fig. 4.7 shows the experimental result of the PSC-VSC under the disturbance of the sudden disconnection of X_{g2} (Type-I transient stability problem). Obviously, the dynamic response of δ is overdamped, which indicates that the PSC-VSC smoothly converge to the new SEP without any overshoot. Therefore, the PSC-VSC does not have the Type-I transient stability problem.

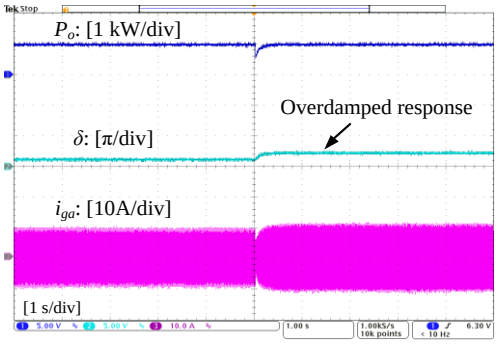

Figure 4.7. Experimental results of the dynamic response of the PSC-VSC after the transient disturbance, where parameters of the test case I listed in Table 4.3 are used. Source: [J3].

Fig. 4.8 shows the experimental results of the PSC-VSC under the three-phase to ground high-impedance fault on X_{g2} (Type-II transient stability problem). The fault is then cleared by disconnecting X_{g2}. Based on the parameters in Table 4.3 and (4.7), the CCT can be calculated as 0.58 s.

Three different scenarios are considered in the experimental tests: 1) the fault is not cleared. 2) the fault is cleared with the FCT=0.7s >CCT. 3) the fault is cleared with FCT=0.5s < CCT. Since there is no equilibrium point during the fault, the LOS is inevitable if there is no fault clearance, as shown in Fig. 4.8 (a). Yet, different from the SG, the PSC-VSC is still capable of re-synchronizing with the power grid after around one cycle of oscillation, even if FCT>CCT, as shown in Fig. 4.8 (b). Of course, the PSC-VSC can always be stabilized if FCT<CCT, as shown in Fig. 4.8 (c). The experimental results in Fig. 4.8 agree well with the theoretical analysis.

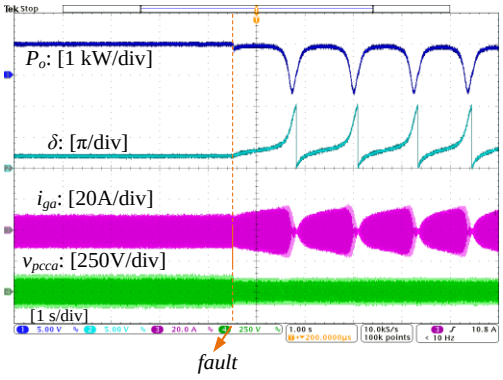

(a)

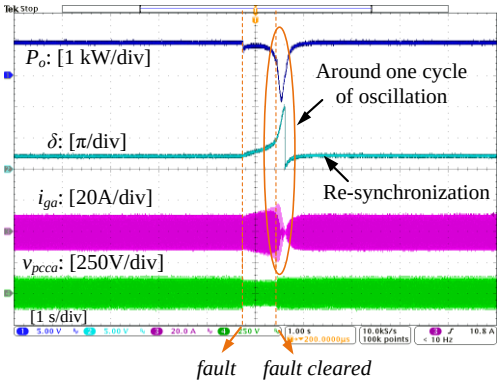

(b)

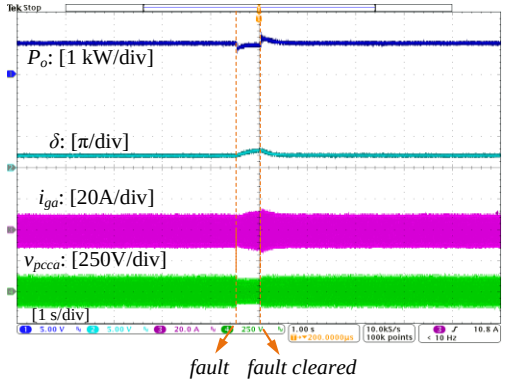

(c)

Figure 4.8. Experimental results of dynamic responses of the PSC-VSC after the transient disturbance, where parameters of the test case II listed in Table 4.3 are used. (a) Fault is not cleared. (b) Fault is cleared with FCT= 0.7s > CCT. (c) Fault is cleared with FCT=0.5s < CCT. Source: [J3].

4.5. Summary

This chapter performs a systematic analysis on the transient stability of the PSC-VSC. The first-order power angle control brings in superior transient stability dynamics of the PSC-VSC over the traditional SG, which are:

- No Type-I transient stability problem.
- Fixed CCA (CCT) for the Type-II transient stability problem.

- Re-synchronization capability even if FCT>CCT.

These superior features of the PSC-VSC could significantly enhance the reliability of the power system.

Chapter 5. Transient Stability of GFL-VSCs with Phase-locked Loop

The content of this chapter is based on **J4, C3 and C4**.

5.1. Background

Nowadays, most of voltage source converters (VSCs) are using the GFL control, where the phase-locked loop (PLL) is adopted for the grid synchronization [11]. Although the concept of the GFM-VSC has been proposed and attracted much attention recently [10], it often needs to be switched to the GFL control during the fault for the overcurrent limitation [40]. Therefore, the stable operation of GFL-VSCs is of vital importance for the reliability and security of the power system.

The small-signal stability of GFL-VSCs has been extensively investigated in literatures [15]-[18], where the negative damping and frequency coupling dynamics introduced by the PLL have been clearly identified. Yet, less research attention has been attracted on the transient stability (synchronization stability under large disturbances) of GFL-VSCs. The real incidents of the unintentional tripping of wind and photovoltaic power plants during the fault have been recently reported [21]-[23], which reveals that GFL-VSCs that operate stably in the steady-state might be destabilized during grid faults (or other large disturbances). Therefore, the transient stability study of GFL-VSCs is urgently demanded.

In [62], it is reported that the PLL cannot synchronize with the power grid if the VSC does not have equilibrium point during the fault. Yet, the loss of synchronization (LOS) might still occur even if there are equilibrium points during the fault, due to the nonlinear dynamics of the PLL [47]-[51]. The straightforward solution to tackle this challenge is to freeze the PLL during the fault [47]. However, the VSC cannot detect the grid phase if the PLL is frozen, which not only affects the correct fault current injection specified by the grid code [46], but also jeopardizes the system dynamics during the fault recovery.

In our work in [J4], a design-oriented transient stability analysis of GFL-VSCs is performed. The transient stability impact of the PLL is thoroughly discussed, and the adaptive-PLL is proposed to guarantee the transient stability and the phase tracking accuracy of the GFL-VSC during the fault. The effectiveness of the proposed method is corroborated by experimental tests. The main content of [J4] is summarized as follows.

5.2. Mathematical Model of GFL-VSCs

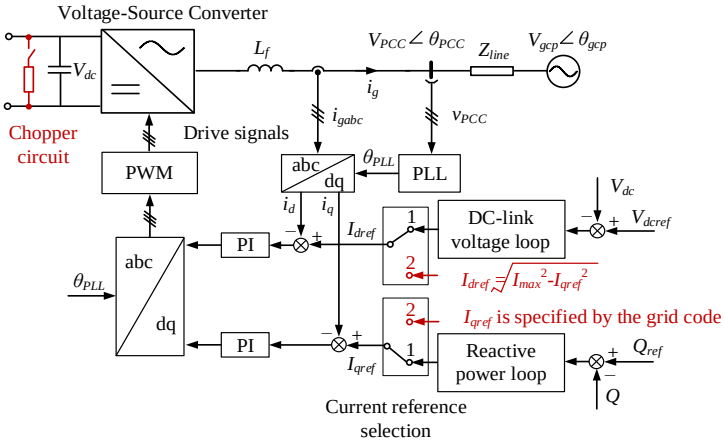

Figure 5.1. A single-line diagram of a GFL-VSC during the normal and fault ride-through operations. The current reference selection is switched to 1 during the normal operation and is switched to 2 during the fault ride through. Source: [J4].

Fig. 5.1 shows the circuit and control diagram of the GFL-VSC. V_{gcp}, θ_{gcp}, V_{PCC} and θ_{PCC} are the magnitudes and phase angles of the grid voltage and the PCC voltage, respectively. The VSC is synchronized with the power grid by means of the PLL, where its output phase angle is denoted as θ_{PLL}. The inner current loop is used to control i_d and i_q to track I_{dref} and I_{qref}, respectively. During the normal operation, I_{dref} is generated by the DC-link voltage loop, while I_{qref} is decided by the reactive power loop [11]. During the grid fault, I_{qref} is specified by the grid code, while I_{dref} is modified accordingly to avoid the overcurrent of the VSC [46], as illustrated in Fig. 5.1.

Since the bandwidth of the inner current loop is usually much higher than that of the PLL, its dynamics can be neglected during the transient stability analysis [63]. Therefore, the VSC shown in Fig. 5.1 can be simplified as the controlled current source, as shown in Fig. 5.2, where φ denotes the phase difference between v_{PCC} and i_g. I_g is the amplitude of the grid current and θ_{line} is the line impedance angle.

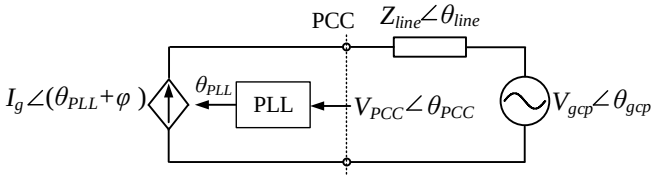

Figure 5.2. The simplified converter-grid system for the transient stability analysis. Source: [J4].

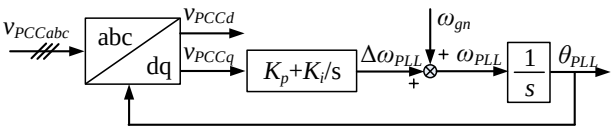

Figure 5.3. Block diagram of the SRF-PLL. Source: [J4].

Fig. 5.3 illustrates the wildly used synchronous reference frame PLL (SRF-PLL) [11], based on which, its dynamic equation can be expressed as

$$\theta_{PLL} = \int \left[\omega_{gn} + \left(K_p + K_i \int \right) v_{PCCq} \right]. \tag{5.1}$$

where ω_{gn} is the nominal grid frequency. K_p and K_i are the proportional and integral gains of the PI regulator of the SRF-PLL, respectively. v_{PCCq} represents the q-axis component of the PCC voltage.

It is known from Fig. 5.2 that v_{PCC} is the sum of the voltage across the line impedance and the grid voltage. This relationship also holds for their q-axis components, i.e.,

$$v_{PCCq} = v_{zq} + v_{gcpq}. \tag{5.2}$$

Considering $Z_{line}=R_{line}+jX_{line}$, v_{zq} and v_{gcpq} can be expressed as

$$v_{zq} = I_d X_{line} + I_q R_{line}. \tag{5.3}$$

$$v_{gcpq} = -V_{gcp} \sin\delta. \tag{5.4}$$

where $\delta = \theta_{PLL} - \theta_{gcp}$.

Substituting (5.2)-(5.4) into (5.1) and considering $\theta_{gcp}=\int \omega_{gn} dt$, which yields

$$\delta = \int \left(K_p + K_i \int \right) \left(I_d X_{line} + I_q R_{line} - V_{gcp} \sin\delta \right). \tag{5.5}$$

Eq. (5.5) characterizes the second-order nonlinear dynamics of the SRF-PLL considering the VSC-grid interactions, based on which, its equivalent diagram can be drawn, as shown in Fig. 5.4.

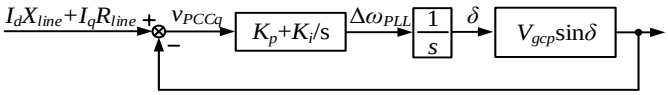

Figure 5.4. The equivalent diagram of the SRF-PLL considering the effect of the line impedance. Source: [J4].

In the steady-state, the grid synchronization is realized by controlling v_{PCCq}=0 [11], i.e.,

$$I_d X_{line} + I_q R_{line} - V_{gcp} \sin\delta = 0 . \tag{5.6}$$

Apparently, the precondition of the system stability is the existence of the solution of (5.6), which requires

$$\left| I_d X_{line} + I_q R_{line} \right| \le V_{gcp} . \tag{5.7}$$

The LOS is inevitable if there are no equilibrium points during grid faults, i.e., (5.7) is not met. It is known from (5.7) that the loss of equilibrium points is more likely to occur under severe grid voltage sags with large grid impedance. Yet, the risk of the LOS persists even if there are equilibrium points during the fault [47]-[51], which will be detailed in the next part.

5.3. Design-oriented Transient Stability Analysis

5.3.1. Two Equilibrium Points during Faults

Fig. 5.5 shows the voltage-angle curves ($V_{gcp}\sin\delta$) of the VSC with two equilibrium points during the fault. The VSC is usually operated with the unity power factor (I_d=I_{max}, I_q=0, which leads to $I_dX_{line}+I_qR_{line} = I_{max}X_{line}$) during the normal operation, and will be switched to the full reactive current injection (I_d = 0, I_q = –I_{max}, which leads to $I_dX_{line} + I_qR_{line} = –I_{max}R_{line}$) during severe faults, as specified by grid codes [46].

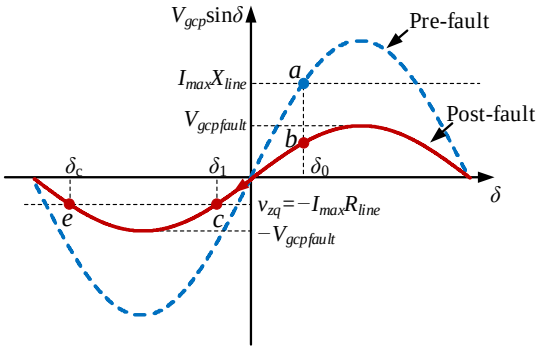

Figure 5.5. Voltage-angle curves of the GFL-VSC when $-I_{max}R_{line} > -V_{gcpfault}$. Source: [J4].

The VSC is initially operated at the stable equilibrium point (SEP) *a*, where $I_{max}X_{line} = V_{gcp}\sin\delta_0$, and then it moves to the point *b* when the fault occurs. The output frequency of the PLL decreases from the point *b* to point *c* due to $-I_{max}R_{line} < V_{gcpfault}\sin\delta_0$ (i.e., $v_{PCCq} < 0$), and then increases from the point *c* to point *e* due to $-I_{max}R_{line} > V_{gcpfault}\sin\delta$ (i.e., $v_{PCCq} > 0$). The stable operation of the VSC requires the output frequency of the PLL to recover to the grid frequency before the unstable equilibrium point (UEP) *e*, otherwise the output frequency of the PLL turns to decrease after the UEP *e* and the LOS is inevitable.

The dynamics of the PLL is characterized by its controller parameters, i.e., the damping ratio (ζ) and the setting time (t_s) [11], which are given by

$$\zeta = \frac{K_p}{2}\sqrt{\frac{V_{gn}}{K_i}}. \tag{5.8}$$

$$t_s = \frac{9.2}{V_{gn}K_p}. \tag{5.9}$$

where V_{gn} is the nominal grid voltage. Eq. (5.5) can be rewritten by applying derivation on both sides of the equation, which leads to

$$\ddot{\delta} = \frac{K_i}{1-K_pI_dL_{line}}\left[I_d\left(\omega_{gn}+\dot{\delta}\right)L_{line} + I_qR_{line} - V_{gcp}\sin\delta\right] - \frac{K_pV_{gcp}\cos\delta}{1-K_pI_dL_{line}}\cdot\dot{\delta}. \tag{5.10}$$

Substituting (5.8) and (5.9) into (5.10), the phase portraits of the VSC with different

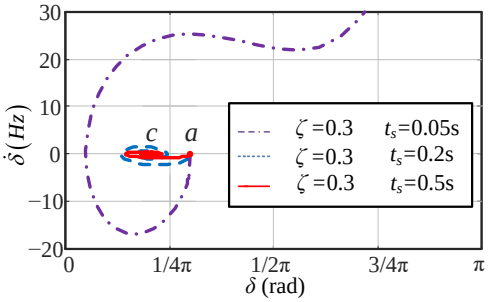

(a)

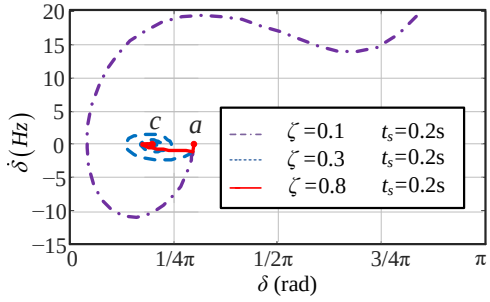

(b)

Figure 5.6. Phase portraits of the VSC when V_{gcp} drops from 1 p.u. to 0.6 p.u. (a) ζ=0.3, t_s=0.05s (unstable), 0.2s (stable), 0.5s (stable). (b) t_s=0.2s, ζ=0.1 (unstable), 0.3 (stable), 0.8 (stable). Source: [J4].

ζ and t_s can be plotted, as shown in Fig. 5.6. The stable and unstable operation of the system are dictated by the convergence (solid and dashed lines) and divergence (dashed-dotted lines) of the phase portraits, respectively. Based on Fig 5.6, two important conclusions can be drawn:

i) The transient stability of the VSC is deteriorated by the reduced t_s of the PLL, as shown in Fig. 5.6 (a). Considering the relationship $X_{line} = \left(\omega_n + \dot{\delta}\right) L_{line}$, Fig. 5.4 can be transformed as Fig. 5.7 with the additional positive-feedback loop. This positive-feedback dynamics is enhanced by the reduced t_s, i.e., larger K_p, which further jeopardizes the transient stability of the VSC. However, when the VSC is operated with the pure reactive current injection (I_d=0) or the grid impedance is resistive (L_{line}=0), the t_s has no impact on the transient stability of the VSC [J4], [C4].

ii) The transient stability of the VSC can be enhanced by the increased ζ of the PLL, as shown in Fig. 5.6 (b). Since the increased ζ helps to dampen the phase overshoot of the PLL, the risk of the VSC from crossing over the UEP *e* during grid faults is reduced [J4], [C4]. Similar conclusions can also be found in SGs, where the better transient stability performance can be obtained with large damping term [1].

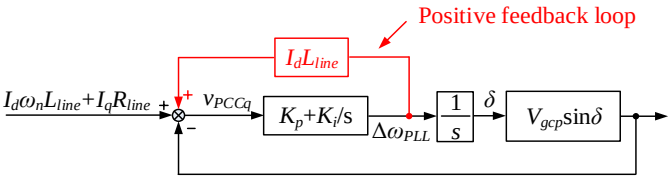

Figure 5.7. Equivalent transformation of the block diagram of the SRF-PLL considering the effect of the frequency-dependent line reactance. Source: [J4].

5.3.2. Single Equilibrium Point during Faults

Fig. 5.8 shows the voltage-angle curves ($V_{gcp}\sin\delta$) of the VSC with single equilibrium point *f* during the fault. In that case, the VSC can only be stabilized if the PLL has the overdamped response, i.e., $\dot{\delta}=0$ at the point *f*.

Eq. (5.5) can be rewritten as

$$\begin{aligned}\dot{\delta} &= \left(K_p + K_i\int\right)\left(I_d X_{line} + I_q R_{line} - V_{gcp}\sin\delta\right)\\ &= \left(K_p + K_i\int\right)\left(-I_{\max}R_{line} - V_{gcpfault}\sin\delta\right) = \dot{\delta}_1 + \dot{\delta}_2\end{aligned}. \tag{5.11}$$

where

$$\dot{\delta}_1 = K_p\left(-I_{\max}R_{line} - V_{gcpfault}\sin\delta\right). \tag{5.12}$$

$$\dot{\delta}_2 = K_i\int\left(-I_{\max}R_{line} - V_{gcpfault}\sin\delta\right). \tag{5.13}$$

It is known from Fig. 5.8 that $-I_{max}R_{line} = -V_{gcpfault}$, and thus, $\dot{\delta}_1 = 0$ holds at the point *f*. However, it can also be observed that $-I_{max}R_{line} - V_{gcpfault}\sin\delta < 0$ before the operating point of the VSC reaches the point *f*, which makes $\dot{\delta}_2 = \int\left(-I_{\max}R_{line} - V_{gcpfault}\sin\delta\right) < 0$ at the point *f*. Therefore, $\dot{\delta} < 0$ is inevitable at the point *f* due to the integral term of the PI regulator of the PLL, which leads to the LOS of the VSC.

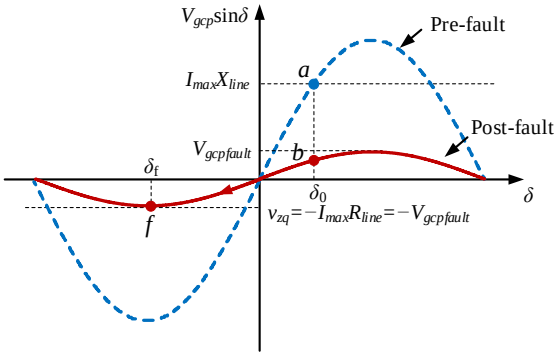

Figure 5.8. Voltage-angle curves of the GFL-VSC when $v_{zq}= -I_{max}R_{line} = -V_{gcpfault}$. Source: [J4].

5.4. Adaptive PLL

As pointed out in 5.3.2, the integral term of the PI regulator of the PLL is the root cause of the LOS of the VSC, without which, $\dot{\delta} = \dot{\delta}_1 = 0$ always holds at the SEP, and thus, the transient stability of the VSC can be guaranteed.

By disabling the integral term of the PI regulator of the PLL ($K_i = 0$), the first-order PLL is yielded. While the first-order PLL brings in better transient stability performance, it cannot accurately track the grid phase angle under the grid frequency drifts [64]. The adaptive-PLL is thus proposed to fully utilize the benefit of the SRF-PLL and the first-order PLL, i.e., the VSC is operated with the SRF-PLL in the steady-state, and only switches to the first-order PLL during the transient dynamic process. By doing so, both the robust transient stability dynamics and the accurate grid phase tracking performance can be guaranteed.

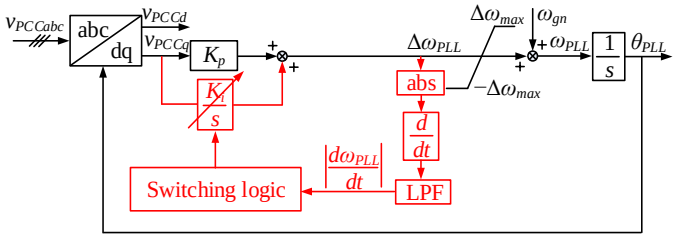

(a)

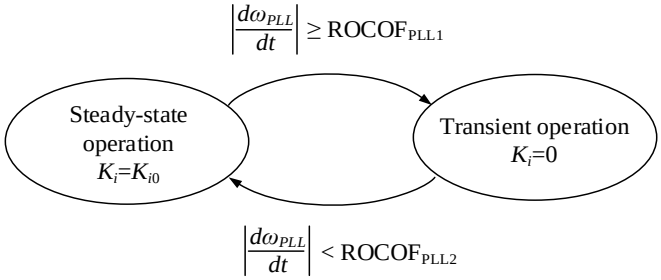

(b)

Figure 5.9. Adaptive-PLL for the transient stability enhancement. (a) Control block diagram. (b) Mode switching logic. Source: [J4].

Fig. 5.9 (a) shows the block diagram of the adaptive-PLL, while its mode switching logic is detailed in Fig. 5.9 (b). The crucial part for implementing the adaptive PLL is the correct identification of the steady-state and the transient state. It is noted that v_{PCCq} ($\Delta\omega_{PLL}$) is almost constant during the steady-state but has an abrupt change during the transient. Therefore, the switching criterion is implemented based on the rate of change of frequency (ROCOF) detected by the PLL, i.e.,

$$\begin{aligned} K_i &= 0, \qquad \left|\frac{d\omega_{PLL}}{dt}\right| \geq \mathrm{ROCOF}_{\mathrm{PLL1}} \\ K_i &= K_{i0}, \qquad \left|\frac{d\omega_{PLL}}{dt}\right| < \mathrm{ROCOF}_{\mathrm{PLL2}} \end{aligned} \quad . \tag{5.14}$$

where K_{i0} is the designed integral gain of PI regulator of the PLL. $|d\omega_{PLL}/dt|$ is obtained by differentiating the absolute value of the output frequency of the PLL, and the low-pass filter (LPF) is used after the differentiation for filtering out the noise. The obtained $|d\omega_{PLL}/dt|$ is then compared with two threshold values $\mathrm{ROCOF}_{\mathrm{PLL1}}$ and $\mathrm{ROCOF}_{\mathrm{PLL2}}$ to determine the operation mode of the PLL, as shown in Fig. 5.9 (b). The selection of $\mathrm{ROCOF}_{\mathrm{PLL1}}$ and $\mathrm{ROCOF}_{\mathrm{PLL2}}$ has been detailed in [J4]. In the experimental test, $\mathrm{ROCOF}_{\mathrm{PLL1}}$ = 5 Hz/s, $\mathrm{ROCOF}_{\mathrm{PLL2}}$ = 0.5 Hz/s are adopted.

Fig. 5.10 illustrates the phase portraits of the VSC with different designed PLLs during grid faults. The parameters are given in Table 5.1 and Table 5.2. It is known from Table 5.1 that the LOS is inevitable if the post-fault voltage is lower than $I_{max}R_{line}$=0.1 pu, due to the absence of equilibrium points.

Fig. 5.10 (a) shows phase portraits of the VSC with 0.14 pu post-fault voltage, where two equilibrium points exist during the fault. It can be seen that the VSC is unstable when using the SRF-PLL with ζ=0.5. Yet, it can be stabilized by increasing ζ to 1.5 or using the adaptive PLL. However, in the case that the post-fault voltage drops to

0.1 pu where only one equilibrium point exists, the VSC can only be stabilized with the adaptive PLL, as illustrated in Fig. 5.10 (b).

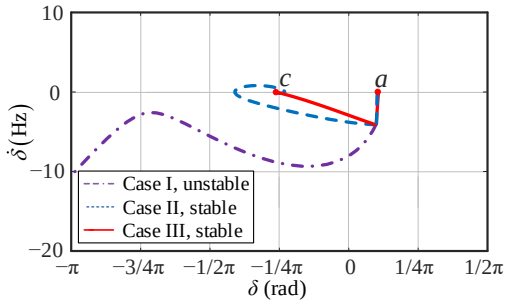

(a)

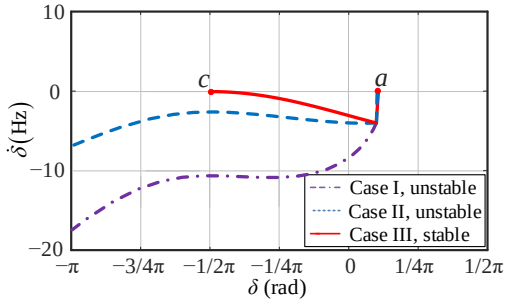

(b)

Figure 5.10. Phase portraits of the VSC with different designed PLLs when V_{gcp} drops. (a) V_{gcp} drops to 0.14 p.u. (b) V_{gcp} drops to 0.10 p.u. Source: [J4].

Table 5.1. Main Circuit Parameters. Source: [J4]

SYMBOL	DESCRIPTION	VALUE (P.U.)
V_{gcprms}	RMS value of the GCP voltage	33 kV (1 p.u.)
P	Power rating of the VSC	1 MW (1 p.u.)
f_g	Grid frequency	50 Hz (1 p.u.)
L_f	Inductance of the output filter	0.096 p.u.
L_{line}	Line inductance	0.28 p.u.
R_{line}	Line resistance	0.1 p.u.

Table 5.2. Controller Parameters of the PLL. Source: [J4]

SYMBOL	CASE I	CASE II	CASE III
PLL structure	SRF-PLL	SRF-PLL	Adaptive-PLL
ζ	0.5	1.5	1.5
t_s	0.1s	0.1s	0.1s

5.5. Experimental Results

The experimental test results are given in this part to verify the theoretical analysis. Table 5.3 illustrates the parameters used in the experimental test, whose per unit values are same as that used in the theoretical analysis. The configuration of the experimental setup is given in Fig. 5.11.

Table 5.3. Main Circuit Parameters used in Experiments. Source: [J4]

SYMBOL	DESCRIPTION	VALUE (P.U.)
V_{gcprms}	RMS value of the GCP voltage	110 V (1 p.u.)
P	Power rating of the VSC	3.6 kW (1 p.u.)
f_g	Grid frequency	50 Hz (1 p.u.)
L_f	Inductance of the output filter	0.096 p.u.
L_{line}	Line inductance	0.28 p.u.
R_{line}	Line resistance	0.1 p.u.

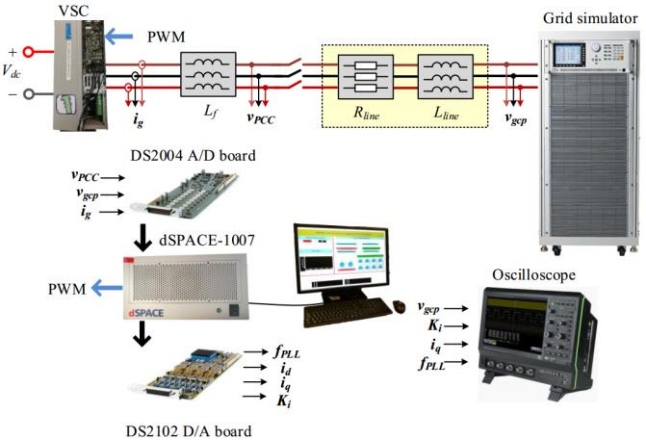

Figure 5.11. Configuration of the experimental setup. Source: [J4].

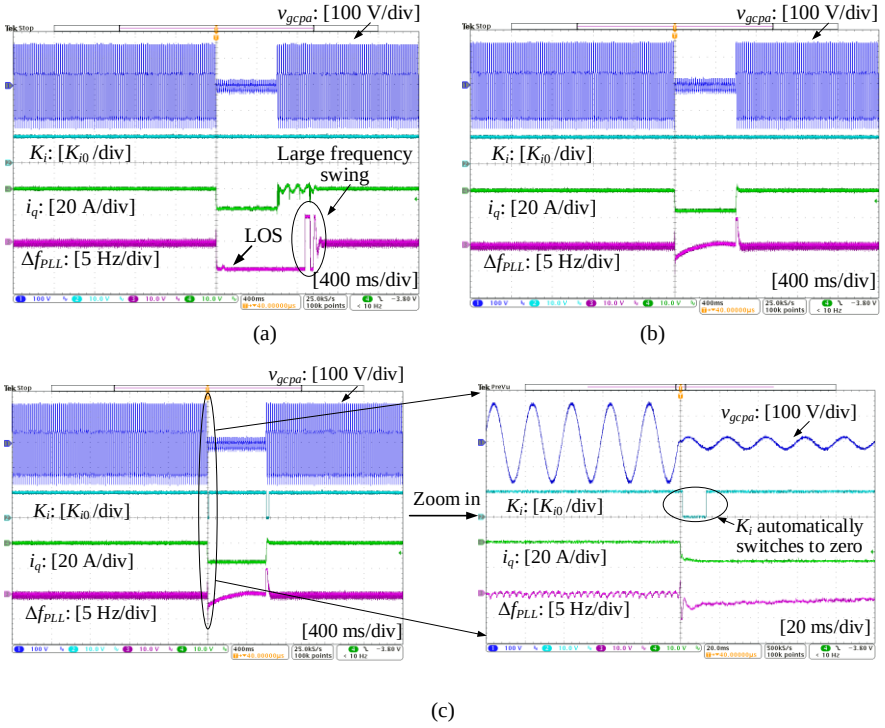

Figure 5.12. Experimental results of the VSC with different designed PLLs during the symmetrical fault, where V_{gcp} drops to 0.14 p.u. (a) Case I: SRF-PLL with ζ=0.5, unstable. (b) Case II: SRF-PLL with ζ=1.5, stable. (c) Case III: Adaptive PLL, stable. Source: [J4].

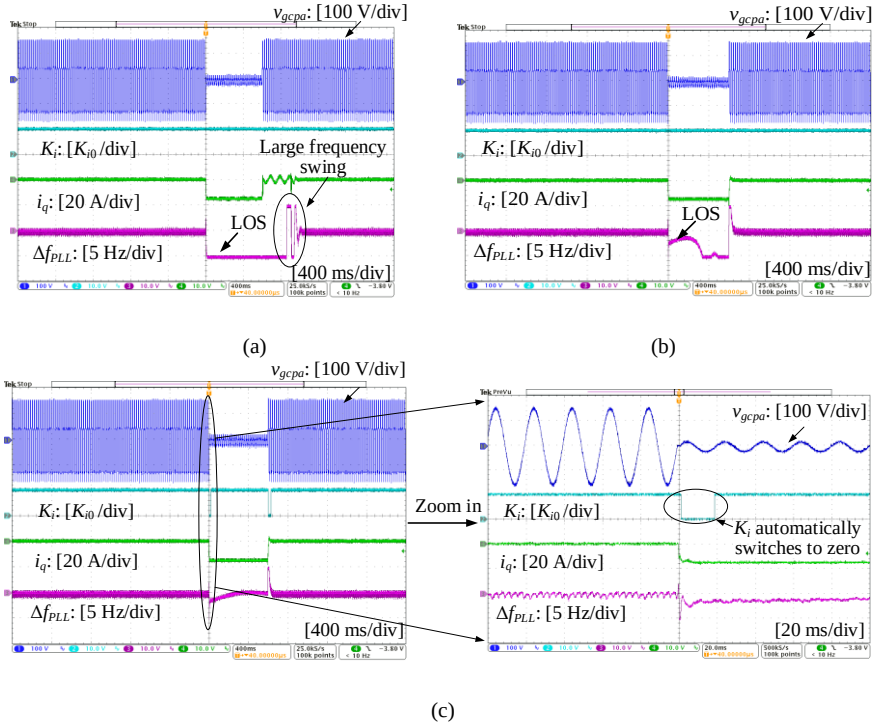

Figure 5.13. Experimental results of the VSC with different designed PLLs during the symmetrical fault, where V_{gcp} drops to 0.10 p.u. (a) Case I: SRF-PLL with ζ=0.5, unstable. (b) Case II: SRF-PLL with ζ=1.5, unstable. (c) Case III: Adaptive PLL, stable. Source: [J4].

Fig. 5.12 shows the test results of the VSC with different designed PLLs when grid voltage drops to 0.14 pu. As illustrated in Fig. 5. 12 (a), the LOS occurs when the VSC is operated with the SRF-PLL (ζ =0.5) during the fault. In contrast, the VSC can operate stably by using the SRF-PLL with the increased ζ (ζ =1.5) or using the adaptive-PLL, as shown in Figs. 5.12 (b) and (c). It should be emphasized that the adaptive-PLL only switches to the first-order PLL during the dynamic process of fault occurrence/recovery, and it will be switched back to the SRF-PLL when the post-fault voltage reaches to the steady-state, as shown in the zoom-in figure of Fig. 5.12 (c). The experimental test results in Fig. 5.12 corroborate the theoretical analysis results given in Fig. 5.10 (a).

Fig. 5.13 illustrates the test results of the VSC with different designed PLLs when grid voltage drops to 0.10 pu. As there is single equilibrium point during the fault. The VSC can only operate stably with the adaptive-PLL, as shown in Fig. 5.13 (c). The experimental test results in Fig. 5.13 corroborate the theoretical analysis results given in Fig. 5.10 (b).

More experimental test results can be found in [J4].

5.6. Summary

This chapter analyzes the transient stability of GFL-VSCs with the PLL. It is revealed that nonlinear voltage-angle dynamics of the PLL may lead to the LOS of the VSC, even if there are equilibrium points during the fault. Moreover, only the first-order PLL can stabilize the VSC during the fault with only one equilibrium point. The adaptive-PLL, which switches between the SRF-PLL and the first-order PLL based on operating conditions, is thus proposed to guarantee the transient stability and phase tracking accuracy of the VSC during the fault. The effectiveness of the proposed method is verified by experimental tests.

Chapter 6. Conclusion and Future Work

6.1. Conclusions

This PhD project performs the design-oriented small-signal stability analysis of MMCs as well as the transient stability analysis of VSCs, the main findings of the PhD project are listed as follows:

- The internal dynamics of the MMC is proven to have a significant impact on its IM in the low-frequency range, which leads to the capacitive centered-diagonal impedance as well as the non-negligible frequency-coupled impedances. The negative damping behavior is further introduced in the centered-diagonal impedance of the MMC when the PR voltage regulator is used, which is the root cause of the low-frequency oscillation of the MMC system with the inductive load. To tackle this challenge, the PIR regulator is used in this PhD project to stabilize the MMC system.

- In order to facilitate analyzing the stability impact of the ZSCC control, the complex-valued small-signal model of the MMC is derived in this PhD project, based on which, the closed-loop SISO ac equivalent impedance of the MMC with/without the ZSCC control is thoroughly compared. The additional resonant peaks are found out in this ac equivalent impedance of the MMC when the ZSCC control is not used, which might interact with the grid impedance and destabilize the MMC. Therefore, the ZSCC control is needed for the stable operation of the MMC system.

- This PhD project reveals that the first-order power angle control can bring in significant benefits on the transient stability of GFM-VSCs, which not only prevents the VSC from the Type-I transient stability problem, but also enables the VSC to re-synchronize with the power grid even if FCT>CCT.

- This PhD project reveals that only the first-order PLL can stabilize the GFL-VSC during grid faults with only one equilibrium point. In order to avoid the drawback of the steady-state phase tracking error of the first-order PLL, the adaptive-PLL that switches between the SRF-PLL and the first-order PLL based on operating conditions, is thus proposed. Theoretical analysis and experimental tests demonstrate that the proposed adaptive-PLL can guarantee both the transient stability and the phase tracking accuracy of the VSC during grid faults.

6.2. Future work

There are still some open questions left unaddressed in this PhD project, which are worth to be investigated in the future.

- The dynamic impacts of the capacitor voltage balancing control and the switching action of the MMC are ignored in this PhD project, which should be considered in the future research to develop a more accurate model of the MMC.

- This PhD project only focuses on analyzing the ac-side dynamics of the MMC, while its dc-side dynamics is not considered. The dc-side dynamics of the MMC is crucial for analyzing the stability of the multi-terminal MMC-HVDC system, in which the dc-links of each MMC station are inter-connected with each other. Therefore, the dc-side dynamics of the MMC is worth investigating in the future research.

- In this PhD project, only the transient stability impact of the APL is considered for GFM-VSCs while only the transient stability impact of the PLL is considered for GFL-VSCs. The transient stability impacts of all other control loops (reactive power control loop, DC voltage control loop, AC voltage control loop, inner voltage/current control loop) should be considered in the future research.

- In this PhD project, the transient stability studies are carried out under a single VSC infinite bus scenario. The future study should focus on more practical system with multiple generation units, including SGs and VSCs with different control schemes.

Bibliography

[1] P. Kundur, *Power System Stability and Control*. New York, NY, USA: McGraw-Hill, 1994.

[2] P. Kundur, J. Paserba, V. Ajjarapu, G. Andersson, A. Bose, C. Canizares, N. Hatziargyriou, D. Hill, A. Stankovic, C. Taylor, T. V. Custem, and V. Vittal, "Definition and classification of power system stability," *IEEE Trans. Power Syst.*, vol. 19, no. 2, pp. 1387–1401, May 2004.

[3] F. Blaabjerg, Y. Yang, D. Yang and X. Wang, "Distributed Power Generation Systems and Protection," *in Proceedings of the IEEE*, vol. 105, no. 7, pp. 1311-1331, July 2017.

[4] C. Buchhagen, M. Greve, A. Menze, and J. Jung, "Harmonic stability—Practical experience of a TSO," in *Proc. Wind Integr. Workshop*, 2016, pp. 1–6.

[5] C. Li, "Unstable operation of photovoltaic inverter from field experiences," *IEEE Trans. Power Del.*, vol. 33, no. 2, pp. 1013–1015, Apr. 2018.

[6] K. Song, *et al*. "High-order harmonic resonances in traction power supplies: A review based on railway operational data, measurements and experience". *IEEE Trans. Power Electron.*, vol. 35, no. 3, pp. 2501–2518, Mar. 2020.

[7] C. Zou, H. Rao, S. Xu, Y. Li, W. Li, J. Chen, X. Zhao, Y. Yang and B. Lei "Analysis of resonance between a VSC-HVDC converter and the AC grid," *IEEE Trans. Power Electron*., vol. 33, no. 12, pp. 10157–10168, Dec. 2018.

[8] X. Wang and F. Blaabjerg, "Harmonic stability in power electronic based power systems: concept, modeling, and analysis," *IEEE Trans. Smart Grid*., vol. 10, no. 3, pp. 2858–2870, May. 2019.

[9] X. Wang, F. Blaabjerg, and W. Wu, "Modeling and analysis of harmonic stability in an AC power-electronics-based power system," *IEEE Trans. Power Electron.*, vol. 29, no. 12, pp. 6421–6432, Dec. 2014.

[10] J. Matevosyan *et al.*, "GFM inverters," *IEEE Power & Energy Magazine*, vol. 17, no. 6, pp. 89–98, November/December 2019.

[11] R. Teodorescu, M. Liserre, and P. Rodriguez, *Grid Converters for Photovoltaic and Wind Power Systems*, Wiley Press, 2011.

[12] E. Vittal, M. O'Malley, and A. Keane, "Rotor angle stability with high penetrations of wind generation," *IEEE Trans. Power Syst.,* vol. 27, no. 1, pp. 353-362, Feb. 2012.

[13] M. Edrah, K. L. Lo, and O.A-Lara, "Impacts of high penetration of DFIG wind turbines on rotor angle stability of power systems," *IEEE Trans. Sustain. Energy*., vol. 6, no. 3, pp. 759–766, July. 2015.

[14] K. Sharifabadi, L. Harnefors, H. Nee, S. Norrga, and R. Teodorescu, Design, *Control and Application of Modular Multilevel Converters for HVDC Transmission Systems*. Hoboken, NJ, USA: Wiley, 2016.

[15] L. Harnefors, M. Bongiorno, and S. Lundberg, "Input-admittance calculation and shaping for controlled voltage-source converters," *IEEE Trans. Ind. Electron*., vol. 54, no. 6, pp. 3323-3334, Dec. 2007.

[16] B. Wen, D. Boroyevich, R. Burgos, P. Mattavelli, and Z. Shen, "Analysis of D-Q small-signal impedance of grid-tied inverters," *IEEE Trans. Power Electron.*, vol. 31, no. 1, pp. 675-687, Jan. 2016.

[17] X. Wang, L. Harnefors, and F. Blaabjerg, "Unified impedance model of grid-connected voltage-source converters," *IEEE Trans. Power Electron., IEEE Trans. Power Electron*., vol. 33, no. 2, pp. 1775-1787, Feb. 2018.

[18] L. Harnefors, X. Wang, A. Yepes, and F. Blaabjerg, "Passivity-based stability assessment of grid-connected VSCs - an overview," *IEEE Jour. Emer. Select. Top. Power Electron.*, vol. 4, no. 1, pp. 116-125, Mar. 2016.

[19] J. Sun and H. Liu. "Sequence impedance modeling of modular multilevel converters," *IEEE J.Emerg. Sel. Topics Power Electron.*, vol. 5, no. 4, pp. 1427-1443, Dec. 2018.

[20] H. Liu, "HVDC converters impedance modeling and system stability analysis," *Ph.D. dissertation*, Rensselaer Polytechnic Institute, 2017.

[21] Joint NERC and WECC Staff Report, "900 MW fault induced solar photovoltaic resource interruption disturbance report," Atlanta, USA, Feb. 2018, [Online]. Available: www.nerc.com.

[22] National Grid, "Technical Report on the events of 9 August 2019," UK, Sep. 2019, [Online]. Available: https://www.nationalgrideso.com/document/152346/download

[23] National Grid, "Appendices to the Technical Report on the events of 9 August 2019." UK, Sep. 2019, [Online]. Available: https://www.ofgem.gov.uk/system/files/docs/2019/09/eso_technical_report_-_appendices_-_final.pdf

[24] J. Lyu, X. Cai, and M. Molinas, "Frequency domain stability analysis of MMC-based HVDC for wind farm integration," *IEEE J. Emerg. Sel. Top. Power Electron.*, vol. 4, no. 1, pp. 141–151, Mar. 2016.

[25] E. Rakhshani and A. M. Cantarellas and D. Remon and P. Rodriguez and I. Candela, "Modeling and control of multi modular converters using optimal LQR controller with integral action," in *2013 IEEE Energy Conversion Congress and Exposition*, Sept 2013, pp. 3965–3970.

[26] J. Lyu, X, Zhang, X. Cai, and M. Molinas. “Harmonic state-space based small-signal impedance modeling of modular multilevel converter with consideration of internal harmonic dynamics,” *IEEE Trans. Power Electron*., vol. 34, no. 3, pp. 2134-2148, Mar. 2019.

[27] Z. Xu, B. Li, S. Wang, S. Zhang, and D. Xu, “Generalized single-phase harmonic state space modeling of the modular multilevel converter with zero-sequence voltage compensation, ” *IEEE Trans. Ind. Electron.*, vol. 66, no. 8, pp. 6416–6426, Aug. 2019.

[28] L. Bessegato, L. Harnefors, K. Ilves, and S. Norrga. *“*A method for the calculation of the AC-side admittance of a modular multilevel Converter*” IEEE Trans. Power Electron*., vol. 34, no. 5, pp. 4161-4172, May. 2019.

[29] L. Bessegato, K. Ilves, L. Harnefors, and S. Norrga. *“*Effects of control on the AC-side ddmittance of a modular multilevel converter*” IEEE Trans. Power Electron*., vol. 34, no. 8, pp. 7206-7220, Aug. 2019.

[30] J. Lyu, X. Cai, and M. Molinas. “Optimal design of controller parameters for improving the stability of MMC-HVDC for wind farm integration,” *IEEE J.Emerg. Sel. Topics Power Electron.*, vol. 6, no. 1, pp. 40-53, Mar. 2018.

[31] Q. Tu, Z. Xu, and L. Xu, “Reduced switching-frequency modulation and circulating current suppression for modular multilevel converters,” *IEEE Trans. Power Del.*, vol. 26, no. 3, pp. 2009–2017, Jul. 2011.

[32] J. W. Moon, C. S. Kim, J. W. Park, D. W. Kang, and J. M. Kim, “Circulating current control in MMC under the unbalanced voltage,” *IEEE Trans. Power Del*., vol. 28, no. 3, pp. 1952–1959, Jul. 2013.

[33] J. Freytes *et al*., “Improving small-signal stability of an MMC with CCSC by control of the internally stored energy,” *IEEE Trans. Power Del.*, vol. 33, no. 1, pp. 429–439, Feb. 2018.

[34] Y. Li *et al*., “Modeling and damping control of modular multilevel converter based dc grid,” *IEEE Trans. Power Syst.*, vol. 33, no. 1, pp. 723–735, Jan. 2018.

[35] K. Ji, G. Tang, J. Yang, Y. Li and D. Liu, “Harmonic stability analysis of MMC-Based DC system using DC impedance model,” *IEEE J.Emerg. Sel. Topics Power Electron.*, early access, 2019.

[36] M. Taul, X. Wang, P. Davari and F. Blaabjerg, “An overview of assessment methods for synchronization stability of grid-connected converters under severe symmetrical grid faults,” *IEEE Trans. Power Electron.*, vol. 34, no. 10, pp. 9655-9670, Oct. 2019.

[37] Q. C. Zhong and G. Weiss, “Synchronverters: Inverters that mimic synchronous generators,” *IEEE Trans. Ind. Electron.*, vol. 58, no. 4, pp. 1259–1267, Apr. 2011.

[38] H. Wu, X. Ruan, D. Yang, X. Chen, W. Zhao, Z. Lv and Q. C. Zhong, "Small-signal modeling and parameters design for virtual synchronous generators," *IEEE Trans. Ind. Electron.*, vol. 64, no. 7, pp. 4292–4303, Jul. 2016.

[39] Z. Shuai, C. Shen, X. Liu, Z. Li and Z. J. Shen, "Transient angle stability of virtual synchronous generators using Lyapunov's direct method, " *IEEE Trans. Smart Grid.*, vol. 10, no. 4, pp. 4648–4661, Jul. 2019.

[40] L. Zhang, L. Harnefors, and H. –P. Nee. *"*Power-synchronization control of grid-connected voltage-source converters*". IEEE Trans. Power Syst., vol*. 25, no. 2, pp. 809−820, May. 2010.

[41] L. Zhang, L. Harnefors and H.-P. Nee, "Modeling and control of VSC-HVDC links connected to island systems" *IEEE Trans. Power Syst*., vol. 26, no. 2, pp. 783−793, May. 2011.

[42] L. Zhang, L. Harnefors, and H. –P. Nee. "Interconnection of two very weak AC systems by VSC-HVDC links using power-synchronization control". *IEEE Trans. Power Syst., vol*. 26, no. 1, pp. 344−355, Feb. 2011.

[43] L. Zhang, H. P. Nee, and L. Harnefors, "Analysis of stability limitations of a VSC-HVDC link using power synchronization control," *IEEE Trans. Power Syst.*, vol. 26, no. 3, pp. 1326–1337, Aug. 2011.

[44] L. Zhang. "Modeling and control of VSC-HVDC links connected to weak AC systems". *PhD Thesis*, KTH, 2011.

[45] J. M. Guerrero, L. G. de Vicuña, J. Matas, M. Castilla, and J. Miret, "A wireless controller to enhance dynamic performance of parallel inverters in distributed generation systems," *IEEE Trans. Power Electron.*, vol. 19, no. 5, pp. 1205-1213, Sep. 2004.

[46] BDEW Technical Guideline, Generating Plants Connected to the Medium-Voltage Network [EB/OL], June 2008 issue.

[47] B. Weise, "Impact of k-factor and active current reduction during fault-ride-through of generating units connected via voltage-sourced converters on power system stability," *IET Renewable Power Generation*, vol. 9, no. 1, pp. 25–36, 2015.

[48] V. Diedrichs, A. Beekmann, and S. Adloff, "Loss of (angle) stability of wind power plants - the underestimated phenomenon in case of very low short circuit ratio," in *Wind Integration Workshop, 2011 Aarhus, Denmark*, October 2011.

[49] S. Ma, H. Geng, L. Liu, G. Yang, and B. C. Pal, "Grid-synchronization stability improvement of large scale wind farm during severe grid fault," *IEEE Trans. Power Syst.*, vol. 33, no.1, pp. 216–226, Jan 2018.

[50] O. Göksu, R. Teodorescu, C. L. Bak, F. Iov, and P. C. Kjær, "Instability of wind turbine converters during current injection to low voltage grid faults and PLL

frequency based stability solution," *IEEE Trans. Power Syst.*, vol. 29, pp. 1683–1691, July 2014.

[51] H. Geng, L. Liu, and R. Li, "Synchronization and reactive current support of PMSG based wind farm during severe grid fault," *IEEE Trans. Sustain. Energy*, vol. 9, no. 4, pp. 1596–1604, Oct 2018.

[52] Y. Hao, X. Yuan, and J. Hu "Modeling of grid-connected VSCs for power system small-signal stability analysis in DC-Link voltage control timescale" *IEEE Trans. Power Syst.*, vol. 32, no. 5, pp. 3981-3991, Sept. 2017.

[53] A. A. Rockhill, M. Liserre, R. Teodorescu, and P. Rodriguez, "Grid-filter design for a multi-megawatt medium-voltage voltage-source inverter," *IEEE Trans. Ind. Electron.*, vol. 58, no. 4, pp. 1205–1217, Apr. 2011.

[54] D. Pan, X. Wang, F. Liu and R. Shi, "Transient stability of voltage-source converters with GFM control: a design-oriented study," *IEEE J. Emerg. Sel. Topics Power Electron.*, early access, pp. 1–1, 2019.

[55] G. Tang, Z. He, H. Pang, X. Huang, and X. Zhang, "Basic topology and key devices of the five-terminal DC grid," *CSEE J. Power Energy Syst.*, vol. 1, no. 2, Jun. 2015.

[56] N. M. Wereley, "Analysis and control of linear periodically time varying systems," *Ph.D. dissertation*, Dept. of Aeronautics and Astronautics, MIT, 1991.

[57] S. R. Hall and N. M. Wereley, "Generalized Nyquist stability criterion for linear time periodic systems," in *Proc. Amer. Control Conf.*, May 1990, pp. 1518–1525.

[58] B. Wen, D. Boroyevich, R. Burgos, P. Mattavelli, and Z. Shen, "Inverse Nyquist stability criterion for grid-tied inverters," *IEEE Trans. Power Electron.*, vol. 32, no. 2, pp. 1548–1556, Feb. 2017.

[59] Y. Zhou, D. Jiang, J. Guo, P. Hu, and Y. Liang, "Analysis and control of modular multilevel converters under unbalanced conditions," *IEEE Trans. Power Del.*, vol. 28, no. 4, pp. 1986–1995, Oct. 2013.

[60] J. Zhou, D. Hui, S. Fan, Y. Zhang, and A. M. Gole, "Impact of short circuit ratio and phase-locked-loop parameters on the small-signal behavior of a VSC-HVDC converter," *IEEE Trans. Power Del.*, vol. 29, no. 5, pp. 2287–2296, Oct. 2014.

[61] Steven H. Strogatz. *Nonlinear Dynamics and Chaos: With Applications to Physics, Biology, Chemistry, and Engineering*. Perseus Books, 1994.

[62] D. Dong, B. Wen, D. Boroyevich, P. Mattavelli, and Y. Xue, "Analysis of phase-locked loop low-frequency stability in three-phase grid-connected power converters considering impedance interactions," *IEEE Trans. Ind. Electron.*, vol. 62, no. 1, pp. 310–321, Jan. 2015.

[63] M. Taul, X. Wang, P. Davari, and F. Blaabjerg, “An efficient reduced-order model for studying synchronization stability of GFL converters during grid faults”, in Proc. *IEEE COMPEL*, June 2019.

[64] S. K. Chung, “A phase tracking system for three phase utility interface inverters,” *IEEE Trans. Power Electron*., vol. 15, no. 3, pp. 431-438, May. 2000.

Appended Publications

Journal Paper I

H. Wu, X. Wang, and Ł. Kocewiak, "Impedance-based stability analysis of voltage-controlled MMCs feeding linear AC systems," *IEEE J. Emerg. Sel. Topics Power Electron*., early access, 2019. DOI: 10.1109/JESTPE.2019.2911654.

Journal Paper II

H. Wu and X. Wang, “Dynamic impact of zero-sequence circulating current on modular multilevel converters: complex valued AC impedance modeling and analysis,” *IEEE J. Emerg. Sel. Topics Power Electron*., early access, 2019. DOI: 10.1109/JESTPE.2019.2951446.

Journal Paper III

H. Wu and X. Wang, “Design-oriented transient stability analysis of grid-connected converters with power synchronization control,” *IEEE Trans. Ind. Electron.*, vol. 66, no. 8, pp. 6473–6482, Aug. 2019.

Journal Paper IV

H. Wu and X. Wang, “Design-oriented transient stability analysis of PLL-synchronized voltage-source converters,” *IEEE Trans. Power Electron.*, vol. 35, no. 4, pp. 3573 - 3589, Apr. 2020.

Conference Paper I

H. Wu, X. Wang, L. Kocewiak, and L. Harnefors, "AC impedance modeling of modular multilevel converters and two-level voltage-source converters: Similarities and differences," in *Proc. IEEE 19th Workshop Control. Model. Power Electron. (COMPEL)*, Jun. 2018, pp. 1–8.

Conference Paper II

H. Wu and X. Wang, “Transient angle stability analysis of grid-connected converters with the first-order active power loop,” in *Proc. IEEE Appl. Power Electron. Conf. Expo.*, Mar. 2018, pp. 3011–3016.

Conference Paper III

H. Wu and X. Wang, “Transient stability impact of the phase-locked loop on grid-connected voltage source converters,” in *Proc. IEEE Int. Power Electron. Conf. (IPEC-ECCE Asia)*, 2018, pp. 2673–2680.

Conference Paper IV

H. Wu and X. Wang, “An adaptive phase-locked loop for the transient stability enhancement of grid-connected voltage source converters,” in *Proc. IEEE Energy Convers. Congr. Expo.*, 2018, pp. 5892–5898.